frontiers

Multi-channel 4D parametrized Atlas of Macro- and Microstructural Neonatal Brain Development

Alena Uus [1,*], **Irina Grigorescu** [1], **Maximillian Pietsch** [2], **Dafnis Batalle** [2,4],

Daan Christiaens [2,5], **Emer Hughes** [2], **Jana Hutter** [2], **Lucilio Cordero Grande** [2,3],

Anthony N. Price [2], **Jacques-Donald Turnier** [2], **Mary A. Rutherford** [2], **Serena J.**

Counsell [2], **Joseph V. Hajnal** [1,2], **A. David Edwards** [2] and **Maria Deprez** [1]

[1] *Biomedical Engineering Department, School Biomedical Engineering and Imaging Sciences, King's College London, St Thomas' Hospital, London, UK*

[2] *Centre for the Developing Brain, School Biomedical Engineering and Imaging Sciences, King's College London, St Thomas' Hospital, London, UK*

[3] *Biomedical Image Technologies, ETSI Telecomunicacion, Universidad Politécnica de Madrid & CIBER-BBN, Madrid, Spain*

[4] *Department of Forensic and Neurodevelopmental Science, Institute of Psychiatry, Psychology & Neuroscience, King's College London, London, UK*

[5] *Department of Electrical Engineering, ESAT/PSI, KU Leuven, Leuven, Belgium*

Correspondence*:
Alena Uus
alena.uus@kcl.ac.uk

ABSTRACT

Structural and diffusion MRI provide complimentary anatomical and microstructural characterization of early brain maturation. The existing models of the developing brain in time include only either structural or diffusion channels. Furthermore, there is a lack of tools for combined analysis of structural and diffusion MRI in the same reference space.

In this work we propose methodology to generate multi-channel (MC) continuous spatio-temporal parametrized atlas of brain development based on MC registration driven by both T2-weighted and orientation distribution functions (ODF) channels along with the Gompertz model (GM) fitting of the signals and spatial transformations in time. We construct a 4D MC atlas of neonatal brain development during 38 to 44 week PMA range from 170 normal term subjects from developing Human Connectomme Project. The resulting atlas consists of fourteen spatio-temporal microstructural indices and two parcellation maps delineating white matter tracts and neonatal transient structures. We demonstrate applicability of the atlas for quantitative region-specific comparison of 140 term and 40 preterm subjects scanned at the term-equivalent age. We show multi-parametric microstructural differences in multiple white matter regions, including the transient compartments. The atlas and software will be available after publication of the article.

Keywords: **multi-modal MRI, neonatal brain, spatio-temporal atlas, atlas-based analysis, multi-channel registration, white matter maturation, white matter parcellation**

1 INTRODUCTION

In addition to being a routine diagnostic tool in neonatal brain imaging (Rutherford et al., 2010), MRI has been widely used for quantification and interpretation of neonatal brain development in term- and preterm-born infants. Premature birth before 37 weeks postmenstrual age (PMA) is associated with an increased risk of atypical brain maturation leading to neurocognitive and neurobehavioural disorders. Multiple studies demonstrated correlation of MRI metrics with prematurity, clinical and environmental factors and neurodevelopmental outcomes (Ball et al., 2017; Barnett et al., 2018; Dimitrova et al., 2020). In this context, models of the normal brain development such as spatio-temporal atlases (Schuh et al., 2018) can also potentially facilitate detection of altered maturation patterns. The advanced acquisition and reconstruction protocols produce high-resolution structural T1-weighted (T1w) and T2-weighted (T2w) MRI volumes that allow segmentation of fine brain anatomical structures (Makropoulos et al., 2014). But these MRI modalities have low contrast for white matter (WM) structures that also varies during the neonatal stage due to the ongoing myelination. On the other hand, lower resolution diffusion MRI reflects the properties of tissue microstructural complexity in terms of diffusivity, anisotropy, neuronal density and fibre orientation (Bastiani et al., 2019; Pietsch et al., 2019). Combined diffusion and structural MRI analysis has already showed a potential to increase interpretability of the brain maturation patterns (Ball et al., 2017).

1.1 Structural MRI metrics

The structural MRI-derived metrics most commonly used in the neonatal brain studies include tissue- and structure-specific volumetry (Kuklisova-Murgasova et al., 2011; Makropoulos et al., 2016; Thompson et al., 2019) and surface measurements such as cortical thickness and curvature (Bozek et al., 2018; Fenchel et al., 2020) that can be extracted from automated segmentations (Makropoulos et al., 2014). Recently, automated segmentation of T2w images has been also applied for quantification of the volume of myelinated regions (Wang et al., 2019). Intensity changes in T1w and T2w images characterize white matter injury (O'Muircheartaigh et al., 2020) and diffuse excessive high signal intensity (DESHI) regions (Morel et al., 2020). Quantitative and semi-quantitative metrics applied to developing neonatal brain include the T1w/T2w signal ratio associated with myelin content (Bozek et al., 2018) and T2 relaxometry (Pannek et al., 2013; Kulikova et al., 2015; Wu et al., 2017; Knight et al., 2018).

1.2 Diffusion MRI metrics

Brain microstructure can be probed using a variety of quantitative metrics derived from diffusion MRI. Even though diffusion tensor imaging (DTI) is limited by inconsistencies in fiber-crossing regions (Jeurissen et al., 2013), DTI-derived metrics, including the fractional anisotropy (FA) and the mean, radial and axial diffusitivity (MD, RD and AD) are still most widely used in the neonatal brain studies (Barnett et al., 2018; Feng et al., 2019; Thompson et al., 2019; Dimitrova et al., 2020). Recently, higher order metrics, that alleviate some of the limitations of the DTI in the fibre crossing regions, have also been applied to investigate neonatal brain development, including the mean kurtosis (MK) index derived from diffusion kurtosis imaging (DKI) (Bastiani et al., 2019) and intracellular volume fraction (ICVF), fiber orientation dispersion index (ODI) and volume fraction of the isotropic compartment (FISO) derived from Neurite Orientation Dispersion and Density Imaging (NODDI) model (Zhang et al., 2012). The NODDI-derived indices have been used to characterize development of both white and gray matter microstructural features (Kunz et al., 2014; Batalle et al., 2019; Kimpton et al., 2020; Fenchel et al., 2020). The microscopic fractional anisotropy (μFA) index (Kaden et al., 2016) designed to disentangle microscopic diffusion anisotropy from the orientation dispersion has not yet been applied to neonatal brain. Constrained spherical deconvolution (CSD) (Tournier et al., 2007) allows extraction of orientation-resolved microstructural

63 information as orientation distribution functions (ODFs) from multi-shell high angular resolution diffusion
64 imaging (HARDI) data. Based on fibre ODFs, fixel-based analysis (Raffelt et al., 2017) provides the means
65 for assessment of specific fibre populations in terms of fibre density (FD) and fibre-bundle cross-section
66 (FC) (Pannek et al., 2018; Pecheva et al., 2019).

1.3   Atlases and models of the neonatal brain development

68 Spatio-temporal normalisation and construction of age-specific group-average templates have been
69 routinely employed in processing pipelines in the recent large neonatal brain MRI studies, to detect
70 inter-group differences and anomalies in individual brains (Oishi et al., 2019). The majority of the reported
71 spatio-temporal population-averaged atlases of the neonatal brain include either structural (T2w and T1w)
72 (Kuklisova-Murgasova et al., 2011; Serag et al., 2012; Wright et al., 2014; Schuh et al., 2014; Makropoulos
73 et al., 2016; Schwartz et al., 2016; Schuh et al., 2018; Wang et al., 2019; O'Muircheartaigh et al., 2020) or
74 diffusion (Feng et al., 2019; Pietsch et al., 2019; Dimitrova et al., 2020) channels. Up to our knowledge, the
75 only existing multi-channel population-averaged T1w+T2w+DTI atlas (Oishi et al., 2011) was constructed
76 from a set of normal term subjects from 38 to 41 weeks PMA. However, the averaged template was reported
77 to have significantly lower sharpness than the original T2w and DTI images. Apart from (Feng et al., 2019)
78 who used FA+MD guided registration, these atlases were constructed using registration driven by a single
79 channel and the output transformations were propagated to the rest. In general, one of the challenges of
80 multi-channel registration is considered to be the alignment between the structural and diffusion MRI
81 volumes. Following spatial normalization, the templates were created using either weighted or direct
82 averaging of the signal in the reference space. Zhang et al. (2016) proposed to perform averaging in the
83 frequency domain and reported higher sharpness of the atlas features.

84 Due to the rapid changes of structure, volume and cytoarchitecture during the fetal and neonatal period, the
85 majority of the atlases have been also resolved in time in the form of weekly templates. Smooth transition
86 between the atlas time points have been provided through kernel regression (Kuklisova-Murgasova et al.,
87 2011; Serag et al., 2012; Schuh et al., 2014, 2018), logistic regression (Wang et al., 2019) or Gaussian
88 process regression (Marquand et al., 2016; O'Muircheartaigh et al., 2020; Dimitrova et al., 2020). Recently,
89 Gompertz model was successfully used to parametrize fetal and neonatal brain volumetry and surface
90 measurements (Wright et al., 2014; Makropoulos et al., 2016; Schwartz et al., 2016), showing better
91 approximation than the linear model (Makropoulos et al., 2016), even though the changes in averaged
92 structural (O'Muircheartaigh et al., 2020) and DTI (Bastiani et al., 2019; Feng et al., 2019; Dimitrova et al.,
93 2020) metrics in WM and GM can be approximated by linear trends. However, so far, there has been no
94 reported works combining structural and diffusion MRI into a spatio-temporal atlas of the normal term
95 born neonatal brain development.

1.4   Region specific analysis

97 The majority of the neonatal brain studies has been employing region-specific quantitative analysis based
98 on correlation between the MRI-derived metrics measured within specific regions and parameters such
99 as gestation age (GA) at birth, clinical factors or neurodevelopmental outcomes. In structural-only MRI
100 datasets segmentation is normally performed by atlas-based methods (Makropoulos et al., 2014). In the
101 WM atlas-based analysis, the parcellation maps for the single-subject or population-average WM DTI
102 atlases (Oishi et al., 2011; Feng et al., 2019; Alexander et al., 2020) were created by 2D manual delineation
103 based on DTI directionally-encoded colour maps for single subject or population-averaged templates. Label
104 propagation based on DTI channel-guided registration has been widely used in neonatal brain studies
105 (Kersbergen et al., 2014; Rose et al., 2014; Wu et al., 2017; Claessens et al., 2019; Feng et al., 2019). The
106 tract-based spatial statistics (TBSS) (Smith et al., 2006) approach uses skeletonized FA maps for definition

107 of the regions (Krishnan et al., 2016; Young et al., 2018; Barnett et al., 2018; Thompson et al., 2019).
108 As an alternative, track-specific analysis employs tractography to identify and segment the major WM
109 pathways (Kulikova et al., 2015; Akazawa et al., 2016; Pecheva et al., 2017; Bastiani et al., 2019; Zollei
110 et al., 2019; Kimpton et al., 2020; Dubner et al., 2020). In this case, the seed regions for tractography are
111 defined in the template space and the segmentations of WM tracts are achieved by thresholding of the
112 resulting probabilistic tractography maps. In Akazawa et al. (2016), this approach was also used to create
113 population-specific average probabilistic maps of the major WM tracts.

1.5 Contributions

115 In this paper we propose to merge multiple metrics extracted from both diffusion and structural MRI in a
116 single parametrized multi-channel spatio-temporal atlas of the normal neonatal brain development.

117 The generated 4D MC atlas covers 37-44 weeks PMA range and includes structural (T1w, T2w and
118 T1w/T2w myelin contrast) and diffusion channels with ODF, DTI, DKI, μFA and NODDI derived metrics.
119 Furthermore, the atlas includes two parcellation maps: (i) the major WM tract regions (Alexander et al.,
120 2020) refined using probabilistic tractography in the template and (ii) the map of the transient WM regions
121 with high maturation rates during neonatal period. To ensure accuracy of spatial alignment, we propose
122 a multi-channel (MC) registration (Uus et al., 2020) guided by spatially-weighted structural, diffusion
123 (ODFs) MRI and cortical segmentation (Makropoulos et al., 2018) channels. Parametrization in time is
124 performed by the Gompertz model (GM) widely used for fitting of growth data. We implemented the
125 atlas construction and fitting functionalities within MRtrix3 software package (Tournier et al., 2019). To
126 demonstrate the application of the proposed atlas we perform multi-modality study to compare term and
127 preterm brain development and identify regions where WM maturation has been altered by preterm birth.

2 MATERIAL AND METHODS

2.1 Cohort, datasets and preprocessing

129 The atlas was constructed using 170 multi-modal MRI datasets of term-born neonates (born and scanned
130 between 37 and 44 weeks PMA) that included T1w, T2w and HARDI scans. Additional 40 datasets of
131 preterm neonates (born between 23 and 32 weeks GA: 28.94 ∓ 2.54 and scanned between 37 and 44 weeks
132 PMA) were used for comparison analysis. Inclusion criteria were high image quality for scans of all
133 modalities, singleton pregnancies and no major brain abnormalities. All scans were acquired under the
134 developing Human Connectome Project (dHCP)[1].The distribution of the GA at birth and PMA at scan is
135 given in Fig. 1.

136 Datasets were acquired on a 3T Philips Achieva scanner equipped with a dedicated 32-channel neonatal
137 head coil and baby transportation system (Hughes et al., 2017). The multi-shell HARDI volumes were
138 acquired with four phase-encode directions on four shells with b-values of $0, 400, 1000$ and $2600\ s/mm^2$
139 with TE $90\ ms$, TR $3800\ ms$ (Hutter et al., 2018; Tournier et al., 2020) with $1.5 \times 1.5 \times 3\ mm$ resolution
140 and $1.5\ mm$ slice overlap and reconstructed to $1.5\ mm$ isotropic resolution using the SHARD pipeline
141 (Christiaens et al., 2021). The structural T2w volumes were acquired using a TSE sequence with TR $12\ s$,
142 TE $156\ ms$. The T1-weighted volumes were acquired using an IR TSE sequence with TR $4.8\ s$, TE $8.7\ ms$.
143 The isotropic T2w and T1w volumes with $0.5\ mm$ resolution were reconstructed using a combination of
144 motion correction (Cordero-Grande et al., 2018) and super-resolution reconstruction (Kuklisova-Murgasova
145 et al., 2012).

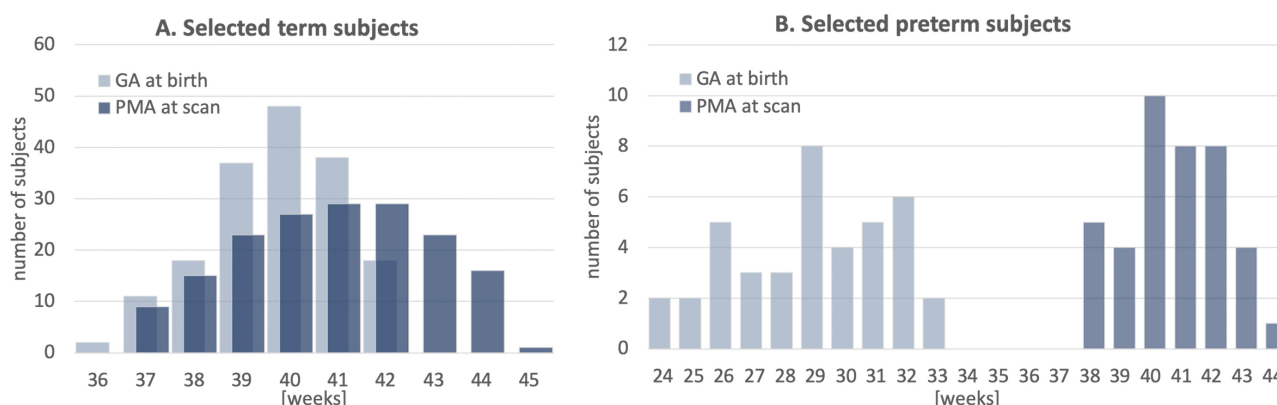[1] dHCP project: http://www.developingconnectome.org

Figure 1. Selected cohort of neonatal subjects from dHCP project: GA at birth and PMA at scan of 170 term subjects **(A)** and 40 preterm subjects **(B)**.

146 Intensities of individual T1w and T2w volumes were bias-corrected and normalised to the same intensity
147 ranges. The brain tissue and structure segmentations were generated by dHCP pipeline (Makropoulos
148 et al., 2014, 2018). For each dataset, the structural and diffusion volumes were coaligned using affine
149 registration of T2w and MD volumes using NCC similarity metric in MRTrix3. The DWI volumes were
150 globally normalised prior to the nonlinear multi-channel registration step (Tournier et al., 2019).

2.2 Extraction of MRI metrics

152 The structural metrics include normalised T1w and T2w intensities as well as the the T1w/T2w ratio
153 thought to be associated with the myelin content (Glasser and Van Essen, 2011). Furthermore, we extracted
154 Jacobians (J) of deformation fields from the MC registration output (Section 2.4) to measure local volumetric
155 changes.

156 The DTI metrics included AD, MD, RD and FA extracted using MRtrix3 toolbox (Tournier et al.,
157 2019). The DKI fitting and calculation of MK was performed similarly to Bastiani et al. (2019). The
158 NODDI (Zhang et al., 2012) toolbox was used for fitting FISO, ICVF and ODI metrics. The estimation
159 of micro FA maps was performed using SMT toolbox (Kaden et al., 2016). Only the two top HARDI
160 shells were used for μFA and DKI fitting in order to minimise the impact of artefacts. In addition, we
161 computed the mean DWI signal mDWI for the top $2600 \ s/mm^2$ shell since it provides high contrast for
162 WM structures. We extracted WM ODF from HARDI using MRtrix3 multi-shell multi-tissue constrained
163 spherical deconvolution (CSD) (Jeurissen et al., 2014). The track density imaging (TDI) maps were
164 generated from the outputs of probabilistic tractography (Tournier et al., 2010) with whole brain as the seed
165 region and 700,000 streamlines for all dataset. This particular number of streamlines was selected arbitrary.

2.3 Multi-channel registration of structural and HARDI MRI

167 In this work, we propose a MC non-linear registration technique to improve accuracy of spatial
168 normalisation. We build on multi-contrast ODF registration framework (Pietsch et al., 2017; Raffelt
169 et al., 2011) which employs SyN Demons (Avants et al., 2007) with an SSD metric and reorientation of
170 ODF using apodized point spread functions (Raffelt et al., 2012). In order to decrease the sensitivity to
171 acquisition or physiology related changes in signal intensities, we propose to replace SSD metric with
172 a novel robust local angular correlation metric for ODF channels based on angular correlation metric
173 introduced in (Anderson, 2005). We further add structural and tissue parcellation channels with local NCC
174 (LNCC) similarity measure. We combine the channels through weighted fusion of the displacement field
175 updates (Forsberg et al., 2011).

176 Angular correlation r_A between two ODFs F^{ODF} and G^{ODF} represented with real valued spherical
177 harmonic (SH) orthonormal basis functions $Y_{lm}(\theta, \phi)$

$$F^{ODF}(\theta, \phi) = \sum_{l=0}^{\infty} \sum_{m=-l}^{l} f_{lm} Y_{lm}(\theta, \phi), \quad G^{ODF}(\theta, \phi) = \sum_{l=0}^{\infty} \sum_{m=-l}^{l} g_{lm} Y_{lm}(\theta, \phi) \tag{1}$$

178 is computed as (Anderson, 2005):

$$r_A = \frac{\sum_{l=2}^{L} \sum_{m=-l}^{l} f_{lm} g_{lm}}{[\sum_{l=2}^{L} \sum_{m=-l}^{l} |f_{lm}|^2]^{\frac{1}{2}} [[\sum_{l=2}^{L} \sum_{m=-l}^{l} |g_{lm}|^2]^{\frac{1}{2}}}, \tag{2}$$

179 where g_{lm} and f_{lm} are the SH coefficients of $G^{ODF}(\theta, \phi)$ and $F^{ODF}(\theta, \phi)$ of order L with even $l = $
180 $\{2, 4, ..., L\}$ harmonic degree terms, correspondingly. The $l = 0$ term does not contribute to AC values.
181 Since this is a correlation metric, the corresponding symmetric updates to the displacement fields Λ^F and
182 Λ^G can be computed in a similar manner to LNCC demons (Avants et al., 2008) but with respect to the 4D
183 ODFs rather than only the 3D local neighbourhood (Eqn. 3).

$$\Lambda^F = \frac{2FG}{F^2 G^2} \left(G - \frac{FG}{F^2} F \right) \nabla F, \quad \Lambda^G = \frac{2FG}{F^2 G^2} \left(F - \frac{FG}{G^2} G \right) \nabla G, \tag{3}$$

184 where $G = \{g_{lm}^n\}_{l=2,...,l_{max},m=-l,...,l}$ and $F = \{f_{lm}^n\}_{l=2,...,l_{max},m=-l,...,l}$ are the vectors of SH coefficients
185 at a given location in the 3D volume space with local neighbourhood $n = 1, ..., N$. We refer to this
186 registration metric as local angular cross-correlation (LAC).

187 The contributions from each of the channels i to the global symmetric displacement field update Λ^{global}
188 are locally weighted with respect to the 3D certainty maps based on the approach proposed in (Forsberg
189 et al., 2011). First, at every iteration, the certainty gradient maps α_i^F and α_i^G are computed from the original
190 volumes F and G for each of the channels (including structural and ODF volumes) and normalised as:

$$\alpha_i^F = \| \nabla F_i^T \nabla F_i \|, \quad \widehat{\alpha}_i^F = \frac{\alpha_i^F}{max(\alpha_i^F)} \tag{4}$$

191 Then, the global symmetric updates to the displacement fields are computed by weighted averaging of
192 the channel-specific update fields with respect to the certainty maps. The sum of all weighted updates is
193 normalized with respect to the sum of the gradient maps.

$$\Lambda_{global}^F = \frac{\sum_i \widehat{\alpha}_i^F \Lambda_i^F}{\sum_i \widehat{\alpha}_i^F}, \quad \Lambda_{global}^G = \frac{\sum_i \widehat{\alpha}_i^G \Lambda_i^G}{\sum_i \widehat{\alpha}_i^G} \tag{5}$$

194 The proposed approach ensures that the output deformation fields are defined by the contribution of the
195 local channel regions with the highest structural content. This is relevant for the ROIs where one of the
196 channels has low intensity contrast. In comparison, the classical multi-variate SyN approach Avants et al.
197 (2007) is based on averaging of the individual channel updates.

2.4 Generation of 4D multi-channel atlas

The 4D parametrized MC atlas of the neonatal brain development was generated from the 170 term neonatal datasets in three sequential steps: (A) initial registration of structural channels to a single structural template and creation of an average multi-channel template, (B) refined registration of structural and diffusion channels to the multi-channel template and creation age-dependent average multi-channel templates, (C) fitting of the signal and deformation fields in time using the Gompertz model to generate parametrized 4D multi-channel atlas. The proposed pipeline is summarised in Fig. 2.

2.4.1 Generation of a 3D multi-channel template

We chose the T2w 36 week template from the dHCP neonatal brain atlas[2] (Schuh et al., 2018) as the global 3D reference space ($Y^{(reforg)}$) due to the lower degree of cortical folding which facilitates more accurate registration of the cortex. All datasets $\{X_i\}_{,i=1,...,N}$ were registered to this template using affine alignment with global NCC followed by non-linear registration guided by two structural channels (T2w + cortex mask), similarly to O'Muircheartaigh et al. (2020):

$$W_i^{(1)} = \mathfrak{D}^{LNCC}(Y_c^{(reforg)}, X_{i,c}), \quad c=\{T2; \ M_{cortex}\};i=1,...,N \tag{6}$$

where $\mathfrak{D}$ is the MC Demons registration operator, $W_i^{(1)}$ are the output deformation warps for each of the N datasets $X_{i,c}$ with $c = \{T2; \ M_{cortex}\}$ channels and $Y_c^{(ref)}$ is the reference volume. The MC registration included spatially weighted fusion of the channels (Sec.2.3, Uus et al. (2020)). The output deformation warps $\{W_i^{(1)}\}_{,i=1,...,N}$ were propagated to the rest of the structural and dMRI channels. The preliminary set of 3D MC templates $\{Y_c^{(1)}\}_{,c=\{T2; \ M_{cortex}; \ normODF\}}$ was generated by averaging of all registered volumes of T2w, cortex mask and normalized ODF channels (Fig. 2A).

2.4.2 Generation of a age-specific multi-channel templates

At the second iteration (Fig. 2B), we used registration with T2w + cortex mask + normalized ODF channels (Sec. 2.3) to align all datasets to the multi-channel template (Sec. 2.4.1):

$$W_i^{(2)} = \mathfrak{D}^{LNCC+LAC}(Y_c^{(1)}, X_{i,c}), \quad c=\{T2; \ M_{cortex}; \ normODF\};i=1,...,N \tag{7}$$

Next, the datasets were divided into 15 subsets according to PMA, to sample the range from 37 to 44 weeks PMA into 0.5 week time-windows. Each of the subsets N^t contains 6-17 subjects depending on availability. The templates $Y_{c,t}^{(2)}$ for each of the metrics (c) described in Section 2.2 were generated by robust weighted averaging the transformed metric maps $X_{i,c}$ in subsets $i \in N^t$:

$$Y_{c,t}^{(2)} = \sum_{i \in N^t} \omega_{i,c} \cdot \Theta(X_{i,c}, W_i^{(2)}) / \sum_{i \in N^t} \omega_{i,c}, \quad t=37,...,44 \tag{8}$$

where Θ is the transformation operator, c is the list of all channels (See Fig. 2C). The voxel-wise weights $\omega_{i,c}$ are binary maps with all values with > 1.5 standard deviations from the mean being excluded in order to minimise the impact of artifacts, cropped regions or misregistrations.

The templates $Y_{c,t}^{(2)}$ are biased towards 36 weeks reference space, we therefore calculate the transformations to remove this bias for each time-point. Because the registration is symmetric, we choose the inverse warps $(W_i^{(2)})^{-1}$ to create the transformation $W_{av,t}^{-1}$ from the global reference space to the
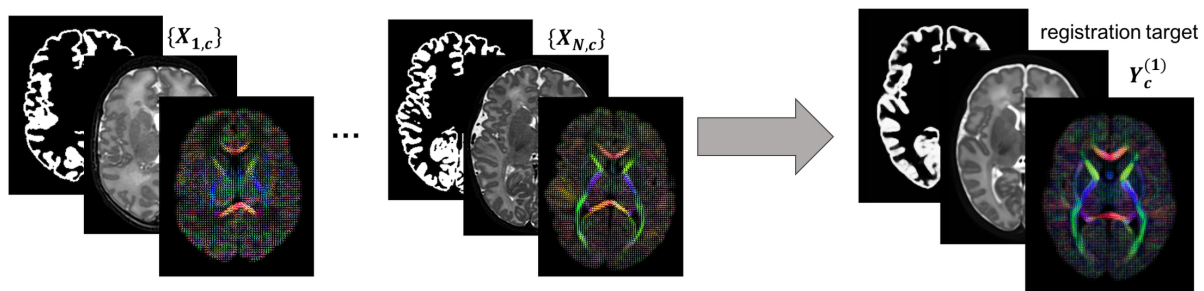
---

[2] dHCP weekly neonatal brain atlas: https://gin.g-node.org/BioMedIA/dhcp-volumetric-atlas-groupwise
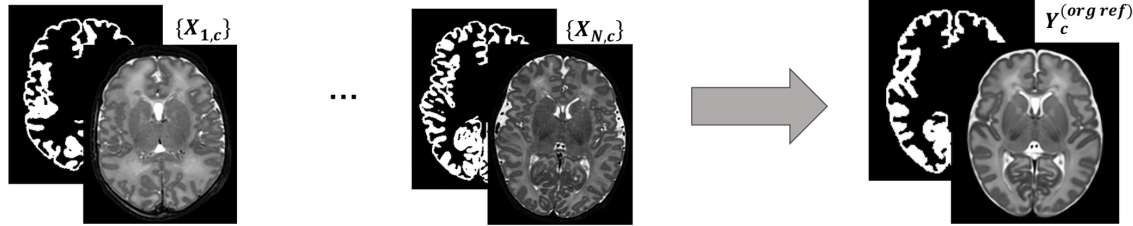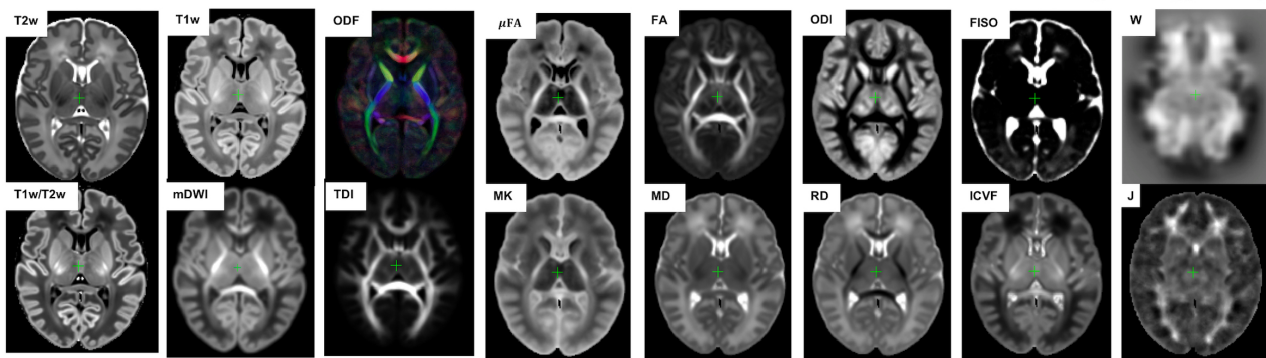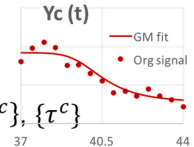
Figure 2. The proposed pipeline for generation of parametrized 4D MC atlas of the neonatal brain development during 37 to 44 weeks PMA range. **A:** (Iteration 1) The T2w + cortex mask guided MC registration to a global reference space $Y^{(ref)}$ (36 weeks T2w dHCP template from Schuh et al. (2018)) is performed for all subjects. Preliminary average templates $Y_c^{(1)}$ are created for T2w, cortex mask and ODF channels. **B:** (Iteration 2) The ODF + T2w + cortex mask guided MC registration to the new multi-channel template is performed of all subjects. Average templates $Y_{c,t}^{(2)}$ are created for all channels and 15 discrete time points. The average inverse nonlinear warps $W_{av,t}^{-1}$ and affine transformations $A_{av,t}^{-1}$ are also created for all 15 time points. **C:** The Gompertz curve fitting in time is performed for all channels and transformations resulting in continuous 4D multi-channel atlas $Y_c^{ref}(t)$ in the reference space the unbiased version $Y_c(t)$.

230 age-specific average space

$$W_{av,t}^{-1} = \sum_{i \in N^t} (W_i^{(2)})^{-1} / N^t, \; t=37,...,44 \tag{9}$$

231 Similarly, we create average inverse affine transformation $A_{av,t}^{-1}$ by selecting only the scaling and sheering
232 components, followed by averaging and inverting.

2.4.3 Parametrized 4D multi-channel atlas

234   In the final step we construct a continuous 4D spatio-temporal multi-channel model of the developing
235 neonatal brain (Fig. 2C) by fitting the Gompertz growth curves to the time-dependent average metric maps
236 and transformations. We propose the following form of the Gompertz function since it allows interpretation
237 of both growth rate (γ) and peak in time (τ):

$$G(t) = (\alpha - \delta)exp(-exp(-\gamma(\tau - t))) + \delta, \tag{10}$$

238 where t is the time point, α and δ control the upper and lower limits of $G(t)$, γ represents the growth rate
239 and τ is the center point corresponding to the growth peak. The model was fitted to the time-dependent
240 average metric maps $Y_{c,t}^{(2)}$ and transformations $W_{av,t}^{-1}, A_{av,t}^{-1}$ using least square minimisation to produce
241 continuous spatio-temporal maps in reference space as well as average inverse transformations:

$$Y_c^{ref}(t) = G(\alpha^c, \delta^c, \gamma^c, \tau^c, t), \; {}_{t=[37;44]} \tag{11}$$

242

$$W^{-1}(t) = G(\alpha^W, \delta^W, \gamma^W, \tau^W, t), \; {}_{t=[37;44]} \tag{12}$$

243

$$A^{-1}(t) = G(\alpha^A, \delta^A, \gamma^A, \tau^A, t), \; {}_{t=[37;44]}, \tag{13}$$

244   where α^c, δ^c, γ^c and τ^c are the interpretable Gompertz model parameters of metrics c = { T1w; T2w;
245 T1w/T2w; mDWI; ODF: SH ODF, TDI; DTI: MD, RD, FA; DKI: MK; NODDI: ODI, FISO, ICVF; μFA;
246 Jacobian} and t is continuous over 37 to 44 weeks PMA range. Unbiased spatio-temporal maps $Y_c(t)$ are
247 obtained by applying nonlinear transformation $W^{-1}(t)$ followed by affine transformation $A^{-1}(t)$ to the
248 biased spatio-temporal maps $Y_c^{ref}(t)$.

2.5 Parcellation of WM regions

250   The dHCP structural atlas (Schuh et al., 2018) already provides parcellations of cortical and subcortical
251 regions, we therefore specifically focus on WM tracts and transient regions. We first propagated the
252 parcellation map of the major WM tract regions from M-CRIB-WM atlas (a single subject template at 41
253 weeks PMA, Alexander et al. (2020)) by registration to our T2w 41 week template $Y_{T2w}^{ref}(41)$.

254   Then we performed the MRTrix3 probabilistic tractography (Tournier et al., 2010) in $Y_{ODF}(41)$ channel
255 for each of the 54 WM regions with propagated labels as seeds. This was followed by manual refinement
256 of all labels in 3DSlicer (Fedorov et al., 2012) based on the thresholded TDI maps for individual tracts and
257 the FA and T2 channels. The procedure was performed in three iterations. The output labels were stored in
258 the atlas reference space resampled to $0.5\,mm$ isotropic resolution to account for finer features.

259   The transient WM regions were localised as regions with high rates of signal changes during 37 to 44
260 weeks PMA. The parcellation was generated semi-automatically from the γ^{av} map obtained by averaging
261 growth rate γ^c for T1w, T2w, RD and FISO channels. The γ^{av} map was thresholded at experimentally
262 selected value 0.25, followed by manual refinement. In addition, the parcellation map was masked with the
263 dHCP atlas cortex mask in order to avoid inclusion of any regions affected by possible misregistrations in
264 the cortex.

2.6   Atlas-based region-specific analysis

In order to assess the application of the proposed approach for the atlas-based region-specific analysis, we performed comparison of term and preterm cohorts. The analysis was based on both the WM and γ^{av} parcellation maps. At first, all subject (selected 40 preterm and 140 term subjects scanned between 38 and 43 weeks PMA range) are registered to the PMA-matched atlas space (Sec. 2.3) with T2w, ODF, cortex and ventricle mask channels. It was identified experimentally, that adding the ventricle mask channel improves registration results for preterm subjects since preterm brains commonly have enlarged ventricles. Therefore, it was used for all subjects in the term-preterm comparison study. The average values for each of the structural and dMRI metrics were computed per each of the investigated regions using weighted averaging with only the values with the difference $< 1.5 \cdot st.dev$ from the mean being included. Then, we assessed the association between the extracted metrics and the PMA at scan and the GA at birth using the ANOVA analysis. The output p-values were corrected for multiple comparisons.

2.7   Implementation details

Taking into account the differences in resolution between the input structural ($0.5\ mm$) and diffusion datasets ($1.5\ mm$), we chose $0.75\ mm$ isotropic resolution as the optimal for the MC atlas. It also should be noted that unlike the previous dHCP atlas (Schuh et al., 2018), the proposed pipeline does not employ Laplacian sharpening of the atlas in order to avoid introducing artificial features into the interpretable maps.

The LAC metric for MC registration of ODF channels was implemented in MRtrix3 (Tournier et al., 2019). In addition, we implemented LNCC Demons metric (Avants et al., 2008) in MRtrix3 for registration of the structural channels. It was experimentally identified that multi-resolution $\{0.5; 0.75; 1.0\}$ and SH order $l_{max} = \{0; 2; 4\}$ schemes and 3 voxel radius for the local neighbourhood for both structural and ODF channels produce high quality for deformable registration of the investigated datasets. We used the standard MRtrix3 regularisation of gradient update with 1 voxel standard deviation and displacement fields based on Gaussian smoothing with 0.75 voxel standard deviation. The proposed 4D GM fitting step (10) was implemented in MRtrix3. The ANOVA analysis for comparison between the term and preterm subjects was performed in RStudio (RStudio Team, 2020) using function `lm`.

3   RESULTS AND DISCUSSION

3.1   Multi-channel registration

We have previously demonstrated that the proposed MC registration improves overall alignment of cortical and WM regions when driven by both structural and ODF channels (Uus et al., 2020). Here we show that adding cortex mask M_{cortex} channel further improves alignment of the cortex. We investigated three scenarios for the MC registration to the reference space (average $Y_c^{ref}(t)$ templates from the generated atlas): (I) $T2w + M_{cortex}$, (II) $T2w + M_{cortex} + FA$, (III) $T2w + M_{cortex} + ODF$ channels and (IV) $T2w + M_{cortex} + ODF M_{ventricles}$ channels. We tested the performance on 12 term datasets from 42.00 to 42.57 weeks PMA range. The alingment was quantitatively assessed by NCC between transformed individual maps and templates $Y_c(t)$ of the corresponding PMA, using the TDI channel in the dilated WM region and T2w channel in the cortex and ventricles regions (highlighted in yellow in Fig.3A).

The $T2w + M_{cortex} + ODF$ MC registration (dark blue) produced the highest NCC within the WM for the aligned TDI maps. It also showed similar results to the structural only registration $T2w + M_{cortex}$ (light blue) within cortex region for the aligned T2 images. This was achieved by the additional cortex mask channel thus resolving the limitation reported in our previous work (Uus et al., 2020). The $T2w + M_{cortex} + FA$ MC registration showed significantly lower NCC potentially due impact of not well defined cortical features in FA map. Both $T2w + M_{cortex} + ODF$ and $T2w + M_{cortex} + FA$ (gray) combinations showed lower
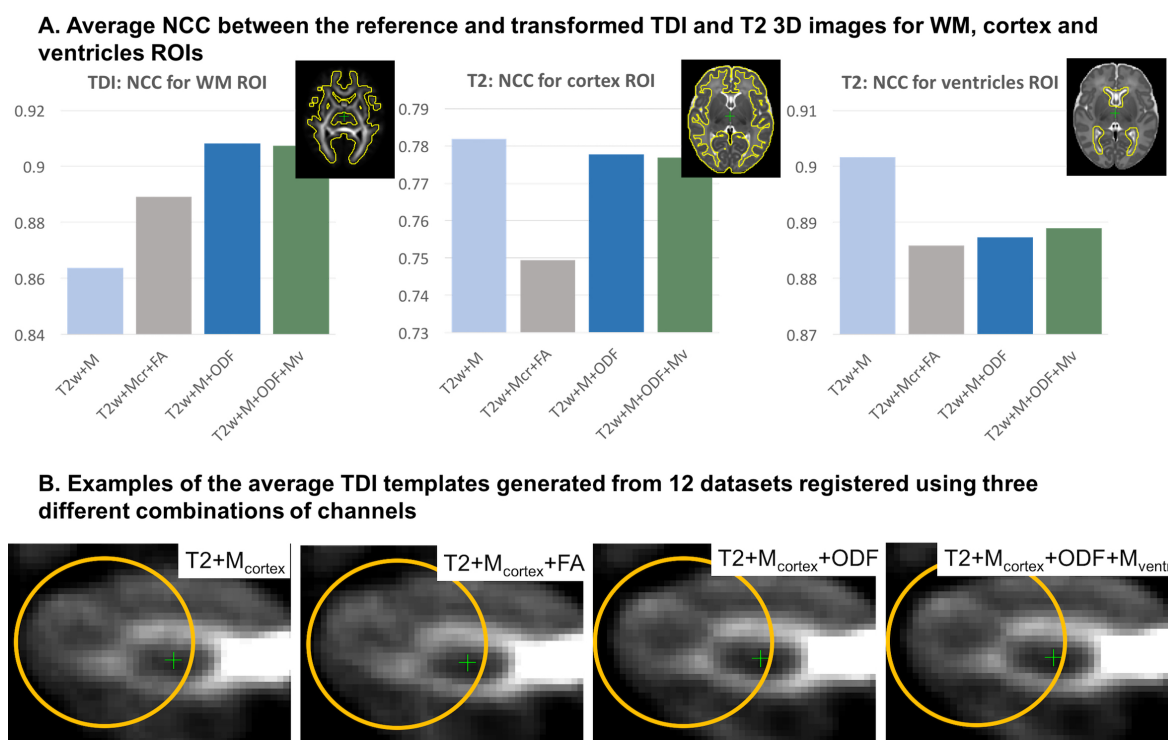
Figure 3. A: Comparison of MC registration results for three combinations of channels: $T2w + M_{cortex}$ (I,light blue), $T2w + M_{cortex} + FA$ (II,gray), $T2 + M_{cortex} + ODF$ (III,dark blue) and $T2 + M_{cortex} + ODF + M_{ventricles}$ (IV,green). The performance was measured by NCC for the WM, cortex and ventricle regions between $Y_c(t)$ and transform TDI map and T2w image. The results are statistically significant with $p < 0.001$ for all cases apart from the combinations I and III for the cortex, II and III for ventricles and III and IV for all regions, which produced similar results. **B:** Examples of the average TDI templates in the cerebellum region generated from the datasets registered using different combinations of channels.

307 performance in the ventricle region. Addition of the ventricles mask only slightly improved the results
308 in several cases. This was primarily due to the fact that the ventricles are quite small and the quality of
309 the segmentation is not sufficient. At the same time, since the preterm subjects commonly have enlarged
310 ventricles, we used it to improve the results for the preterm cohort study in the atlas-based analysis
311 (Sec.2.6,Sec.3.4). The advantage of the $T2w + M_{cortex} + ODF$ MC registration is demonstrated visually
312 by better defined average TDI map of the cerebellum shown in Fig.3B.

313 **3.2   4D multi-channel atlas of normative neonatal brain development**

314   The resulting multi-channel 4D atlas $Y_c^{ref}(t)$ in the reference space (36 weeks PMA dHCP atlas (Schuh
315 et al., 2018)) is given in Fig. 4. Unbiased atlas $Y_c(t)$ obtained after application of average inverse warps for
316 38, 41 and 44 weeks PMA time points is presented in Fig. 5. We can observe nonlinear changes due to
317 cortical folding in the T2w templates. Volumetric expansion/contraction due to growth the is visible in the
318 Jacobian maps.

319   The WM parcellations map with 54 ROIs created in the atlas reference space (Sec. 2.5) for the region-
320 specific analysis of the metric values is shown in Fig. 6. The label annotation information follows the
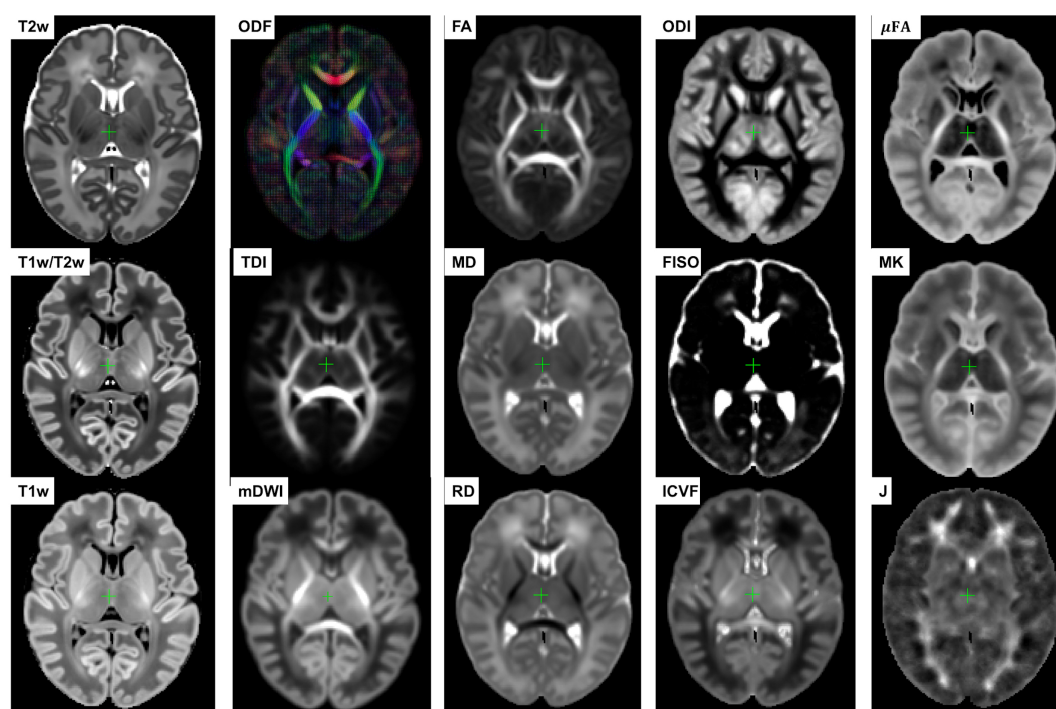321 original annotations in Alexander et al. (2020).

Figure 4. Multi-channel 4D atlas in the reference space (corresponding to 36 weeks PMA). Structural channels: T1, T2, T1/T2 and Jacobian; ODF channels: SH ODF, mDWI, TDI; DTI channels: MD, RD, FA; DKI channel: MK; NODDI channels: ODI, FISO, ICVF; μFA.
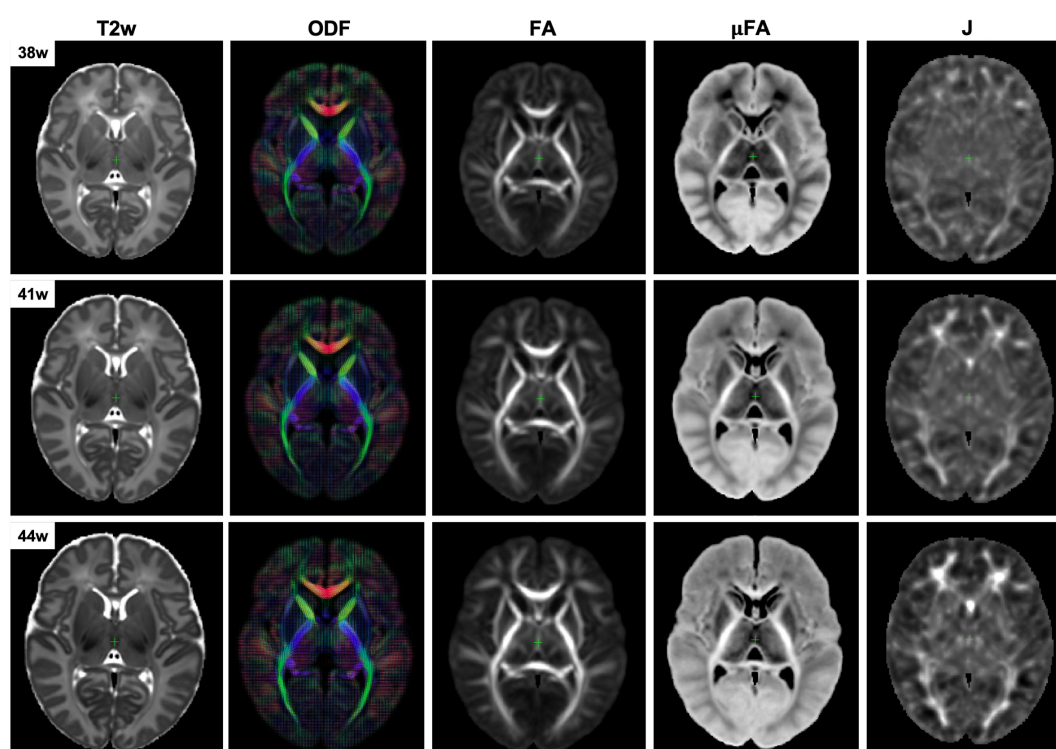

Figure 5. Example unbiased 4D atlas channels at 38, 41 and 44 weeks PMA. The corresponding Jacobian maps (J) are shown in the reference space.
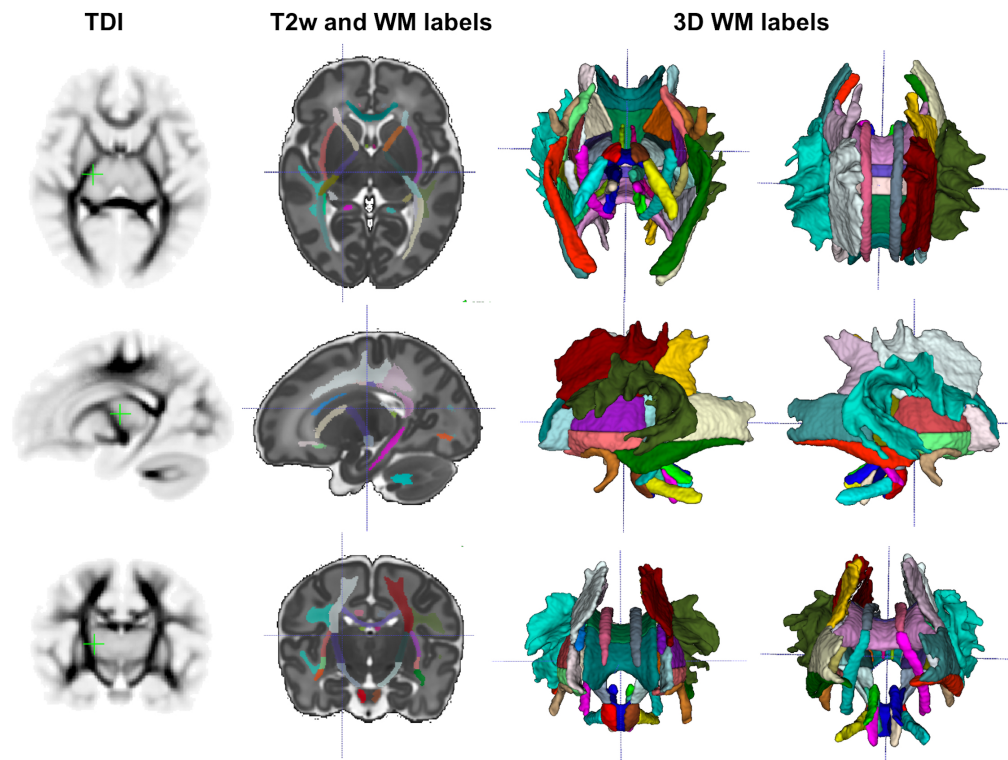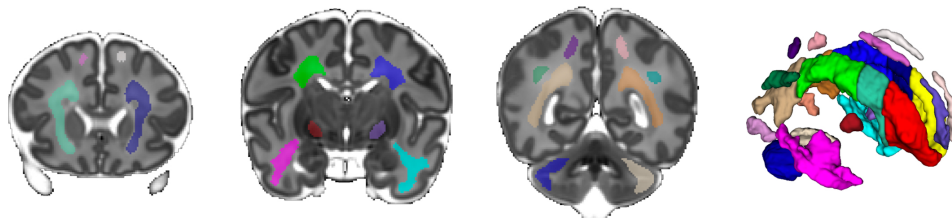
Figure 6. The WM parcellation map in the atlas reference space. The 54 ROIs are based on the structures defined in the M-CRIB-WM atlas (Alexander et al., 2020). The corresponding TDI map highlights the WM pathway regions.
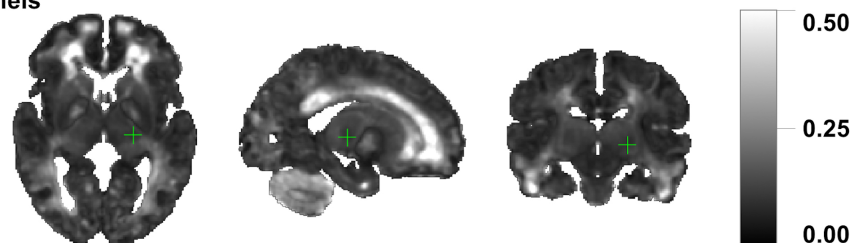

Figure 7. A: The parcellation map of 24 paired regions identified by high change rates during 37 to 44 week PMA. **B**: The average maturation rate map γ^{av} computed from T1w, T2w, RD and FISO channels.

322   Fig. 7.A presents the parcellation map of the transient regions identified by high rates of signal changes
323 during 37 to 44 week PMA segmented from the average γ^{av} map (Fig. 7.B). The parcellation map has 24
324 regions with the majority being consistent with the transient fetal compartment regions described in the
325 recently introduced extended MRI scoring systems of cerebral maturation (Pittet et al., 2019) including
326 periventricular crossroads, Von Monakow WM segments and subplate. We also identified fast developing
327 regions within the cerebellum and subcortical grey matter.

328   We also calculated R^2 scores to evaluate the Gompertz model fit. Our results confirmed that GM offers
329 higher R^2 scores than linear regression with p<0.001 for the combined γ and WM parcellation map region.
330 The primary regions where the GM fitting outperformed linear fitting corresponded to the γ^{av} parcellation
331 map (0.662∓0.189 vs. 0.652∓0.190 with p<0.001) with the high signal change rates. Examples of non-
332 linear patterns are shown in Figures 9-11. Relatively small improvement in R^2 however suggests, that
333 linear fit offers reasonable approximation during this time-window.

334 3.3 Visual analysis of normal neonatal brain development

335   Fig. 8 shows probabilistic tractography generated from the ODF channel and the corresponding T1w
336 channel (in the reference space) in the frontal WM region at 38, 41 and 44 weeks PMA time points.
337 The increase in the T1w signal (known to be sensitive to proliferation of cells and myelin precursors
338 and decreasing water content (Girard et al., 2012)) can be linked to the developing WM pathways seen
339 in tractography (highlighted in red circle). The graphs show the corresponding increasing intensities in
340 age-specific average templates $Y_{c,t}^{(2)}$ and fitted signal values $Y_c^{ref}(t)$ of the TDI and T1w channels computed
341 in the small Von Monakow WM segment (Pittet et al., 2019) highlighted in yellow in the T1w channel.
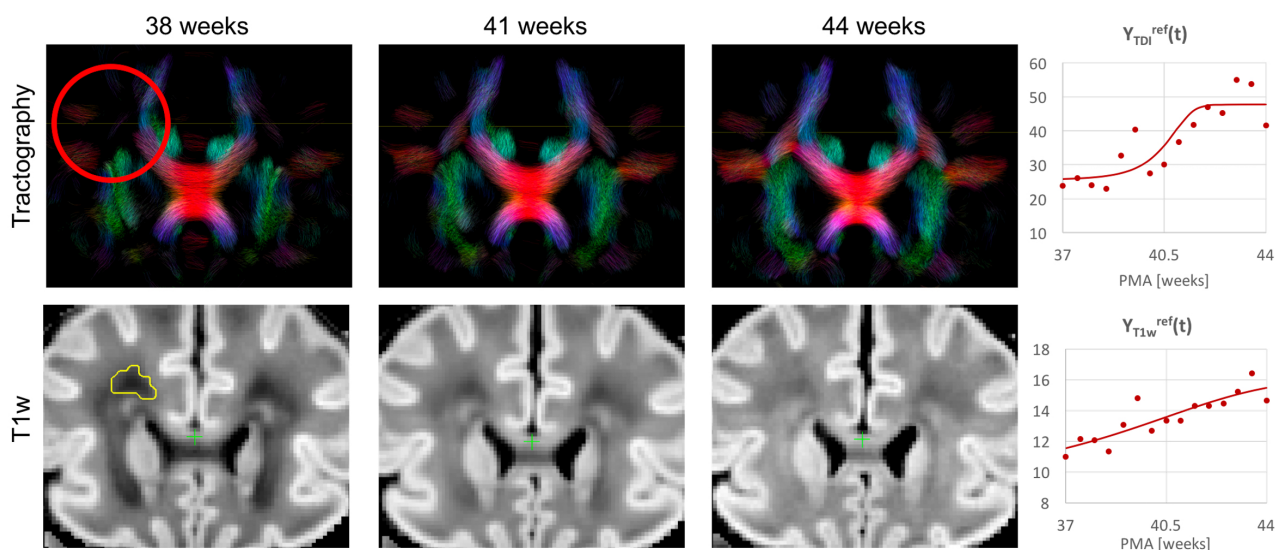

Figure 8. Whole brain probabilistic tractography generated from the ODF channel and the corresponding T1w channel (in the reference space) in the frontal WM region at 38, 41 and 44 PMA weeks time points. The developing WM pathway (red circle) can be linked to increasing T1w signal intensity (yellow region). The graphs show the signal in age-specific templates $Y_{c,t}^{(2)}$ and fitted Gompertz model $Y_c^{ref}(t)$ in the TDI and T1w channels averaged over the region highlighted in yellow.

342   Figures 9-11 show examples of the signal intensity changes in time and the corresponding growth rate
343 maps γ^c. The regions highlighted in yellow have significant growth peak offsets in time (≥ 0.2 weeks from
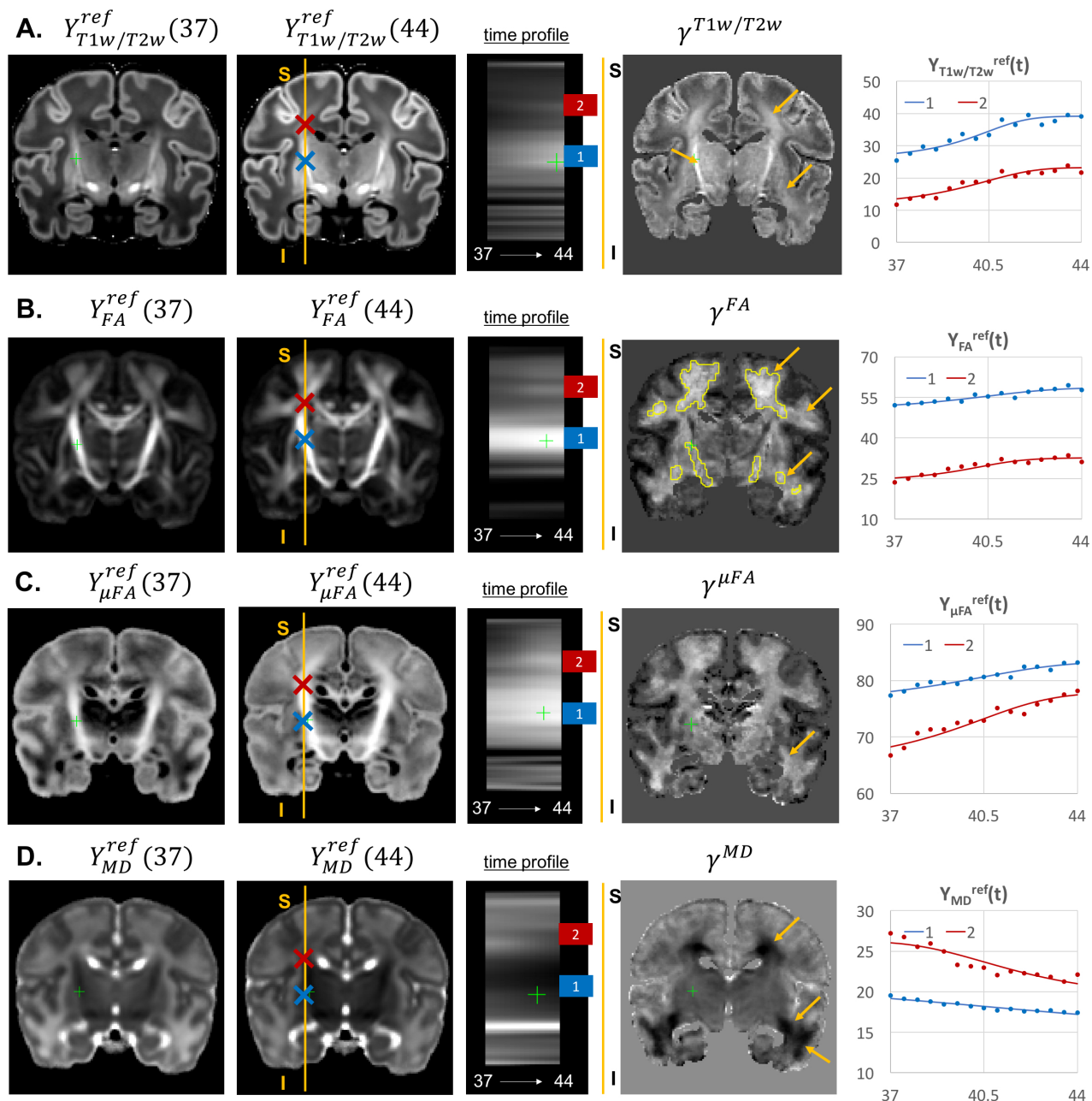344 the 40.5 weeks central time point) in τ^c. The graphs show average signal values in 15 discrete age-specific

Figure 9. Examples of the signal changes in time (in the reference space) in T1w/T2w (**A**), FA (**B**), μFA (**C**) and MD (**D**) channels. First column: 37 week template. Second column: 44 week template. Third column: signal change in time. Fourth column: γ^c maps. Fifth column: Signal change in time in age-specific templates $Y_{c,t}^{(2)}$ and fitted Gompertz model $Y_c^{ref}(t)$ computed over 3x3x3 voxel regions in two locations: PLIC (blue) and superior corona radiata (red). The regions highlighted with yellow contours have significant growth peak offset in τ^c.

345 templates $Y_{c,t}^{(2)}$ and the corresponding fitted signal $Y_c^{ref}(t)$ calculated within small 3x3x3 voxel regions at
346 specific locations, including the right posterior limb of internal capsule (PLIC), superior corona radiata,
347 periventricular crossroads, corpus callosum, Von Monakow WM segment and cerebellum.
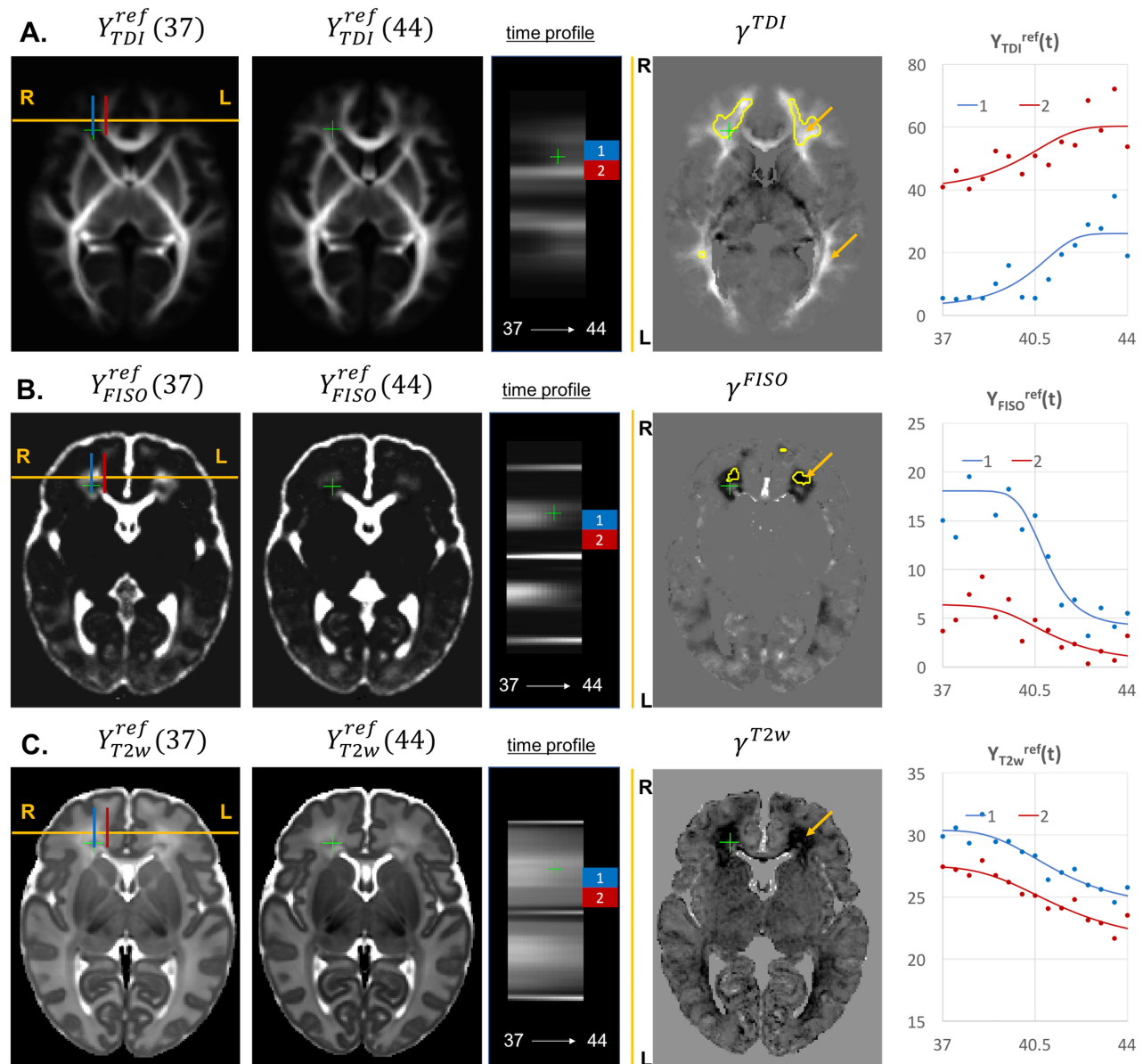
Figure 10. Examples of the signal changes in time (in the reference space) in TDI **(A)**, FISO **(B)** and T2w **(C)** channels. First column: 37 week template. Second column: 44 week template. Third column: signal change in time. Fourth column: γ^c maps. Fifth column: Signal change in time in age-specific templates $Y_{c,t}^{(2)}$ and fitted Gompertz model $Y_c^{ref}(t)$ computed over 3x3x3 voxel regions in two locations: prefrontal corpus callosum (red) and Von Monakow WM segment (blue). The regions highlighted with yellow contours have significant growth peak offset in τ^c.

348   The WM tracts are characterized by different maturation times and rates (Iida et al., 1995). The T1w/T2w
349 contrast (linked to myelination by Glasser and Van Essen (2011)) shows signal increase from 37 to 44
350 weeks (Fig. 9.A). The $\gamma^{T1w/T2w}$ map and the average signal graphs $Y_{T1w/T2w}(t)$ confirm that the rate
351 of T1w/T2w signal increase is the highest in the PLIC region (blue) and the corona radiata (red). The
352 $\tau^{T1w/T2w}$ parameter of the Gompertz model is 40.5 weeks in both regions which is agreement with
353 the previously reported myelination milestones (Counsell et al., 2002; Wang et al., 2019). There is also
354 a noticeable increase in the cortical T1w/T2w signal, also previously reported by Bozek et al. (2018),
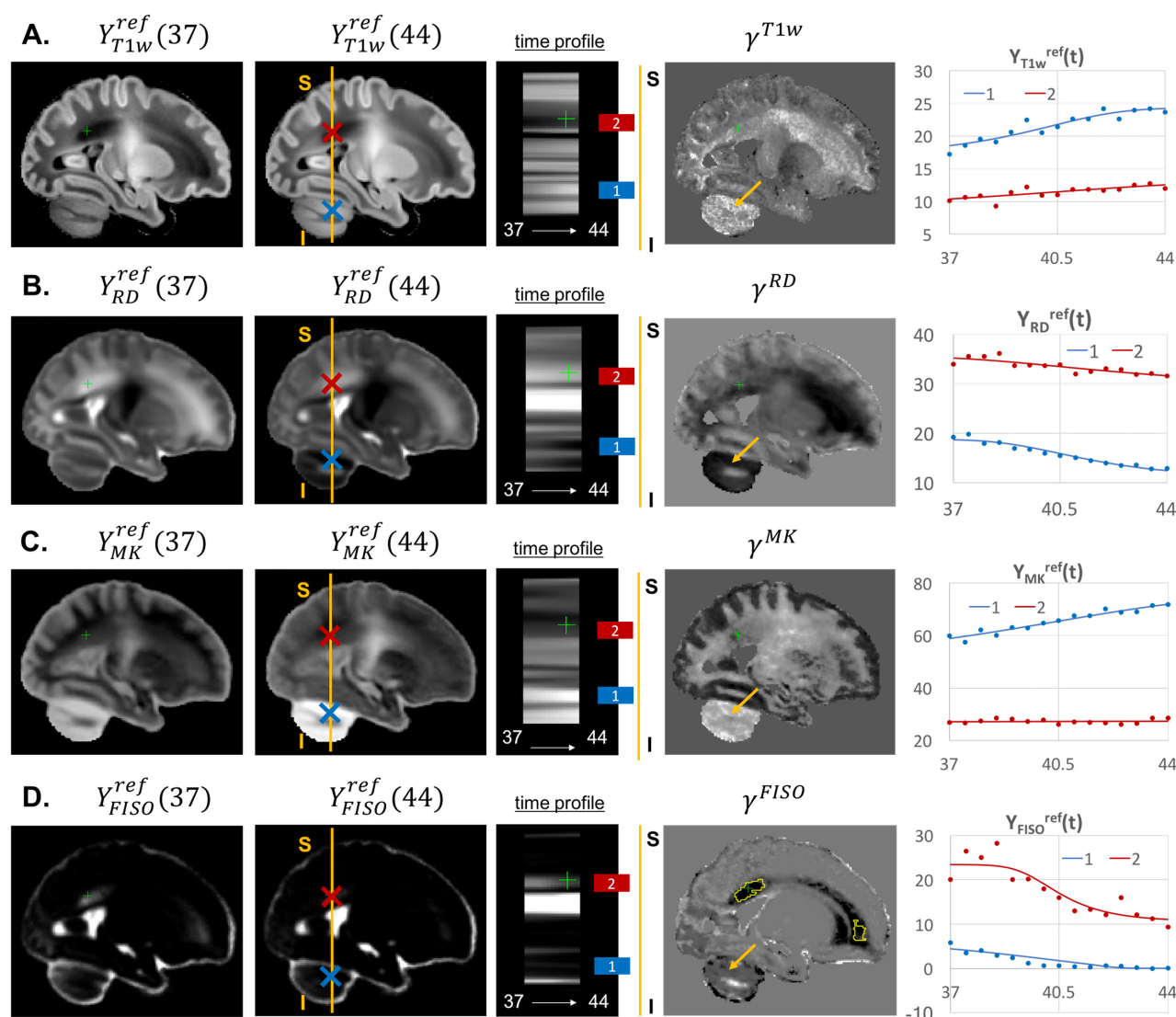
Figure 11. Examples of the signal changes in time (in the reference space) in T1w (**A**), RD (**B**), MK (**C**) and FISO (**D**) channels. First column: 37 week template. Second column: 44 week template. Third column: signal change in time. Fourth column: γ^c maps. Fifth column: Signal change in time in age-specific templates $Y_{c,t}^{(2)}$ and fitted Gompertz model $Y_c^{ref}(t)$ computed over 3x3x3 voxel regions in two locations: cerebellum (blue) and periventricular crossroads (red). The regions highlighted with yellow contours have significant growth peak offset in τ^c.

355 which may be due to myelination or the increased cell density (Girard et al., 2012). Both FA and μFA
356 signals (Fig.9.B-C) gradually increase in all WM regions in agreement with the trends reported in (Feng
357 et al., 2019). The μFA map shows generally higher degree of changes than FA, potentially due to the
358 increasing crossing fiber effect, while in γ^{FA}, the more prominent WM changes are observable primarily
359 in the corona radiata, sagittal stratum and superior longitudinal fasciculus (highlighted with arrows).
360 The γ^{MD} map of the MD channel (Fig.9.D) shows high decrease in the superior corona radiata, sagittal
361 stratum and the transient fetal compartments associated with WM maturation (Pittet et al., 2019) including
362 the periventricular crossroads and subplate regions (highlighted with arrows). The MD signal is slowly
363 decreasing the PLIC region as can be seen in the corresponding graph (blue). All of the presented γ^c maps

364 also show significant changes in the periventricular parietal crossroad regions (highlighted with arrows)
365 with the significant decrease in MD and increasing in T1w/T2w.

366   Given the fixed number of streamlines used for probabilistic tractography, there is a notable redistribution
367 of the TDI amplitude from the main to proximal WM tracts (Fig 10.A). The corresponding growth rate γ^{TDI}
368 map is positive in the frontal (anterior corona radiata) and thalamic radiation WM regions (highlighted with
369 arrows) and negative in the internal capsule. The R-L time profile in the frontal region (Von Monakow WM
370 segment, blue) shows the increased track density at 44 weeks. The average TDI signals $Y_{TDI}^{ref}(t)$ in this
371 region (blue) and the corpus callosum (red) are also characterized by a significant degree of nonlinearity.
372 NODDI FISO component (Fig. 10.B) shows a prominent reduction in the same frontal region which is
373 in agreement with the expected decrease of water content and progressing maturation of WM pathways
374 (Girard et al., 2012). Similarly to TDI, the average FISO signals $Y_{FISO}^{ref}(t)$ in the investigated WM ROIs
375 have nonlinear shape with the steep decrease the occurring during the 39.5-43 weeks period. Similar
376 decrease is observed in T2w signal (Fig. 10.C). The FISO channel in the sagittal view in Fig. 11.D also
377 demonstrates similar patterns in the periventricular crossroads (red).

378   Most of the channels also show prominent changes in the cerebellum associated with normal maturation
379 (Fig.11, blue). The T1w signal intensity $Y_{T1w}^{ref}(t)$ is gradually increasing due to WM maturation along with
380 the increasing microstructural complexity reflected in the MK channel with the high γ^{MK} map values
381 and the expected decreasing trends of the RD $Y_{RD}^{ref}(t)$ and FISO $Y_{FISO}(t)$ signals (potentially due to the
382 decreasing amount of free water (Girard et al., 2012)).

383   3.4   Atlas-based region-specific analysis

384   We performed ANOVA analysis to assess influence of GA at birth on microstructure of WM regions
385 delineated in our new atlas, with PMA as a cofounding variable. In order to assess the feasibility of using
386 the ANOVA analysis for the investigated datasets, we performed linear fitting for each of the channels. The
387 γ^c values showed high correlation with the linear slope maps with the average NCC for all channels in the
388 whole brain ROI 0.903∓0.085 (without CSF). This confirms that during 37 to 44 weeks PMA range linear
389 approximation is acceptable.

390   Fig.12 visualises WM and transient regions in selected channels where average signal value was
391 significantly associated with GA at birth. We found significant association of multiple indices with
392 GA in the corona radiata, superior longitudinal fasciculus, corpus callosum and thalamic radiation. The
393 T1w/T2w contrast was also significantly associated with GA in the internal and external capsules (Fig.12.A).
394 We also found significant association of GA with γ^{av} parcellation regions (Fig.12.B), which is in agreement
395 with the prolonged existence of transient compartments in preterm subjects (Kostović and Judaš, 2006).

396   Fig.13.A highlights differences in rate of maturation in γ^c maps between term and preterm cohorts.
397 The graphs in Fig.13.B show the average signal values in the frontal right Von Monakow WM segment
398 (highlighted in yellow in the γ^c maps). There is a clear increasing trend in T1w/T2w, FA and TDI for
399 the term cohort along with the decreasing FISO and RD. However, the slopes for the preterm cohort are
400 close to zero with high variance in the signal values. Furthermore, in this region, the preterm subjects are
401 characterized by the significantly higher FISO and RD values and lower T1w/T2w, TDI and FA than the
402 term cohort at the 42-43 week PMA period. This is consistent with the commonly reported lower FA and
403 higher diffusivity values in preterm groups (Hermoye et al., 2006; Knight et al., 2018; Dimitrova et al.,
404 2020), again suggesting delayed maturation of transient compartments in premature babies (Kostović and
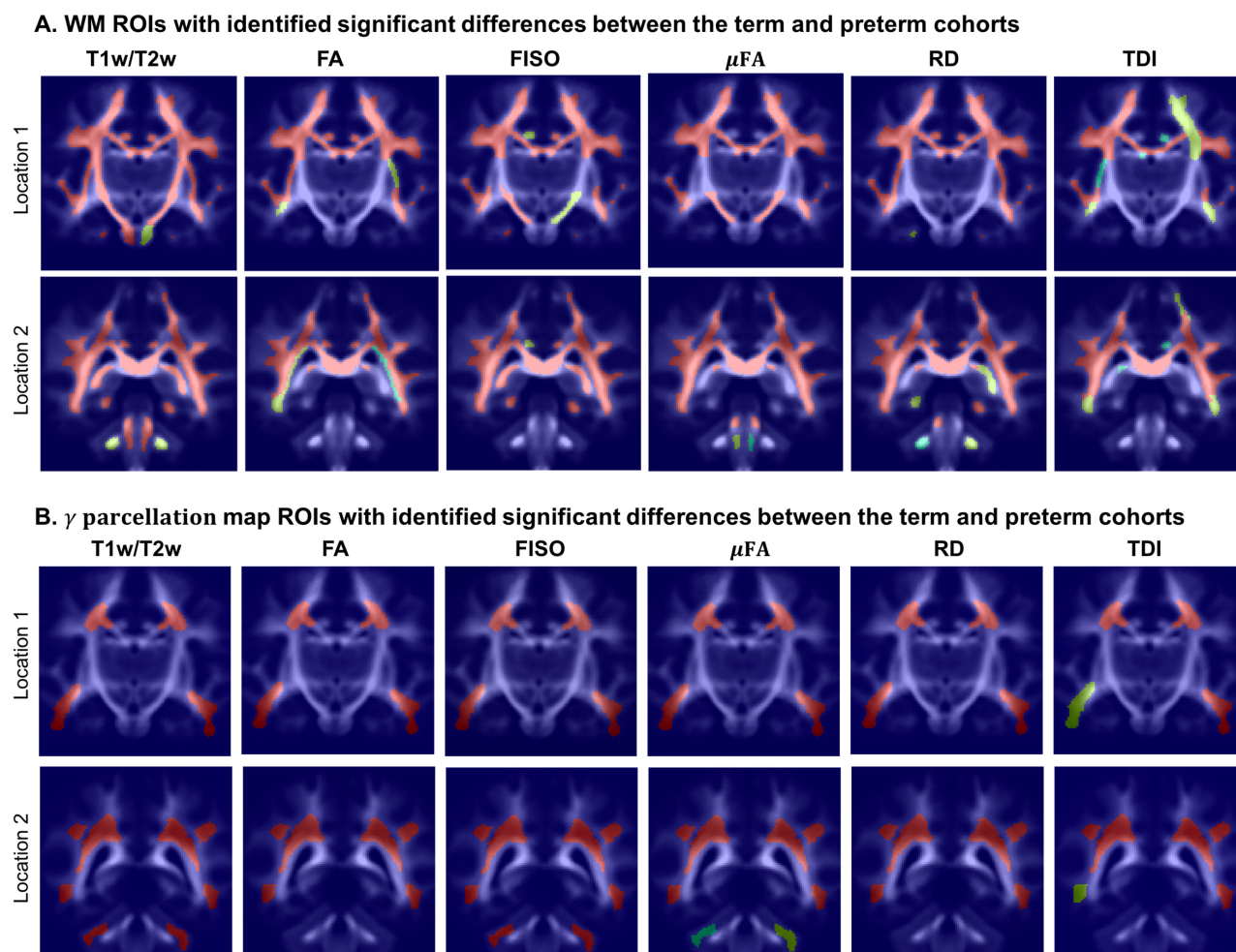405 Judaš, 2006).

Figure 12. Atlas-based region-specific analysis. The regions significantly associated with GA at birth are highlighted with red ($p < 0.001$), yellow ($p < 0.01$) and green ($p < 0.05$) and overlaid over the averaged TDI map in two coronal view locations. **A**: WM parcellation regions. **B**: γ^{av} parcellation regions.

4 LIMITATIONS AND FUTURE WORK

406 The generated atlas is specific to dHCP acquisition protocols, which might limit application in terms of
407 comparison with the datasets from other studies. However, the proposed tools can be easily applied to
408 generate study- and acquisition-specific 4D MC atlases. We investigated relatively narrow neonatal period,
409 and extension wider age range would improve reliability of Gompertz model fit and bring more insights
410 into early brain development.

411   The study comparing term and preterm brain development included only 40 preterm subjects and they
412 were not grouped with respect to specific types of anomalies, which can be addressed in future as more
413 datasets become available. Including additional cortical and sub-cortical regions could also enrich the
414 insights into normal and preterm microstructural brain development.

5 CONCLUSIONS

415 In this work, we proposed and implemented a novel pipeline for generation of continuous 4D multi-channel
416 atlases. It is based on MC ODF+T2w guided registration and the Gompertz model fitting of both signal
417 intensities and spatial transformations. The MC registration pipeline implemented in MRtrix3 employs the

A. Maturation γ^c maps for the term and preterm cohorts

B. Average signal values in the Von Monakow WM segment (highlighted by yellow in the γ^c maps) for the term and preterm cohorts
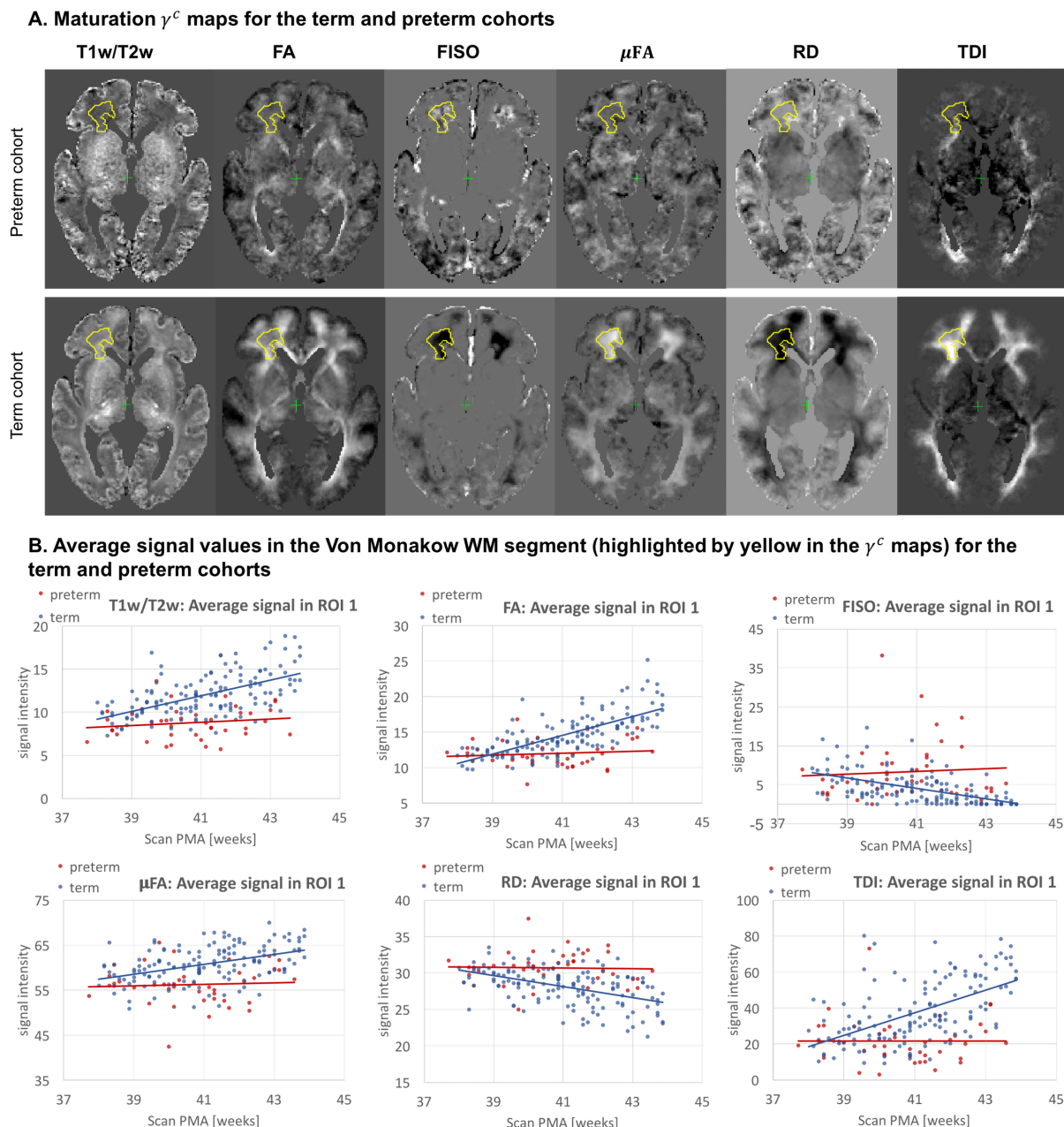

Figure 13. Atlas-based analysis: comparison of the term (140) and preterm cohorts (40) for 38 to 43 weeks scan PMA range for a subset of channels c={ T1w/T2w; TDI; RD; FA; FISO; μFA }. **A**: The γ^c maps of GM fitting for the term and preterm cohorts for 38 to 43 weeks PMA range. **B**: The mean signal values in the frontal WM ROI from the $\gamma^{average}$ parcellation map (highlighted in yellow in the gamma maps) for the term (blue) and preterm (red) cohorts for 38 to 43 weeks PMA range.

418 novel LAC similarity metric for ODF channels, LNCC metric for structural T2w and weighted fusion of
419 the updates to the displacement fields. It also includes the cortex mask channel for better alignment of the
420 cortex regions.

421   Based on the proposed methods, we generated a first continuous multi-channel atlas of the normal
422 term neonatal brain development during 37 to 44 weeks PMA range generated from 170 subjects from
423 dHCP project. The atlas contains 15 channels including structural (T1w, T2w and T1w/T2w contrast) and

424 DWI-derived metrics based on ODF, DTI, DKI, μFA and NODDI models. The GM fitting of the signal
425 intensity and spatial transformation components in 4D allowed parametrization of the atlas. The output
426 γ maps representing the rate of change can be used for interpretation of how maturation processes are
427 manifested in different structural and diffusion MRI-derived metrics.

428 We also found that the fetal transient compartments (Pittet et al., 2019) have high contrast in the T2w,
429 T1w, FISO, MD, RD and TDI γ^c maps.

430 The atlas also includes detailed WM parcellation maps: (i) the map with the major WM tract ROIs based
431 on the definitions from the recently introduced M-CRIB-WM neonatal atlas (Alexander et al., 2020) and
432 (ii) the map of the regions associated with the high γ signal change rates during the normal WM maturation
433 process. We tested the applicability of these parcellation maps for region-specific atlas-based studies on
434 comparison between the term and preterm cohorts. We found significant effects linked to prematurity in
435 the multiple WM regions including the transient fetal compartments. The atlas and the software tools are
436 publicly available to support future studies of early brain development.

CONFLICT OF INTEREST STATEMENT

437 The authors declare that the research was conducted in the absence of any commercial or financial
438 relationships that could be construed as a potential conflict of interest.

AUTHOR CONTRIBUTIONS

439 A.U. prepared the manuscript, implemented the code for the extended MC registration, fitting and analysis,
440 generated the 4D MC atlas and conducted the experiments. I.G. participated in implementation of the
441 preprocessing and analysis code, the design of the study and interpretation of the results. M.P. developed
442 the original code for SSD MC ODF registration in MRtrix3. B.D. performed preprocessing of the dHCP
443 datasets. M.P., D.C. and J.D.T developed the tools for preprocessing and analysis of HARDI dHCP datasets.
444 J.H., E.H., J.D.T, L.C-G. and A.P. developed MRI acquisition protocols for the neonatal dHCP datasets.
445 L.C-G. developed the tools for preprocessing of structural dHCP datasets. J.V.H., A.D.E., S.C. and M.R
446 are coordinators of the dHCP project. MD conceptualised the study and the methods, obtained the funding
447 and supervised all stages of the research and preparation of the manuscript. All authors gave final approval
448 for publication and agree to be held accountable for the work performed therein.

FUNDING

ACKNOWLEDGMENTS

SUPPLEMENTAL DATA

DATA AVAILABILITY STATEMENT

459 The generated MC atlas including all 4D fitted signal map channels, fitted 4D transformations, output GM
460 fitting maturation map and both WM and γ parcellation maps together with the software tools used to
461 generate the atlas will be available online after publication of the article.

462 The preprocessed datasets analyzed in this study will become available after the public release of the
463 dHCP data.

REFERENCES

464 Akazawa, K., Chang, L., Yamakawa, R., Hayama, S., Buchthal, S., Alicata, D., et al. (2016). Probabilistic
465   maps of the white matter tracts with known associated functions on the neonatal brain atlas: Application
466   to evaluate longitudinal developmental trajectories in term-born and preterm-born infants. *NeuroImage*
467   128, 167–179. doi:10.1016/j.neuroimage.2015.12.026
468 Alexander, B., Yang, J. Y. M., Yao, S. H. W., Wu, M. H., Chen, J., Kelly, C. E., et al. (2020). White
469   matter extension of the Melbourne Children's Regional Infant Brain atlas: M-CRIB-WM. *Human Brain*
470   *Mapping* 41, 2317–2333. doi:10.1002/hbm.24948
471 Anderson, A. W. (2005). Measurement of fiber orientation distributions using high angular resolution
472   diffusion imaging. *MR in Medicine* 54, 1194–1206
473 Avants, B. B., Duda, J. T., Zhang, H., and Gee, J. C. (2007). Multivariate normalization with symmetric
474   diffeomorphisms for multivariate studies. In *MICCAI 2007*. vol. 4791 LNCS, 359–366
475 Avants, B. B., Epstein, C. L., Grossman, M., and Gee, J. C. (2008). Symmetric diffeomorphic image
476   registration with cross-correlation: Evaluating automated labeling of elderly and neurodegenerative brain.
477   *Medical Image Analysis* 12, 26–41
478 Ball, G., Aljabar, P., Nongena, P., Kennea, N., Gonzalez-Cinca, N., Falconer, S., et al. (2017). Multimodal
479   image analysis of clinical influences on preterm brain development. *Annals of Neurology* 82, 233–246.
480   doi:10.1002/ana.24995
481 Barnett, M. L., Tusor, N., Ball, G., Chew, A., Falconer, S., Aljabar, P., et al. (2018). Exploring the
482   multiple-hit hypothesis of preterm white matter damage using diffusion MRI. *NeuroImage: Clinical* 17,
483   596–606. doi:10.1016/j.nicl.2017.11.017
484 Bastiani, M., Andersson, J. L., Cordero-Grande, L., Murgasova, M., Hutter, J., Price, A. N., et al. (2019).
485   Automated processing pipeline for neonatal diffusion MRI in the developing Human Connectome Project.
486   *NeuroImage* 185, 750–763. doi:10.1016/j.neuroimage.2018.05.064
487 Batalle, D., O'Muircheartaigh, J., Makropoulos, A., Kelly, C. J., Dimitrova, R., Hughes, E. J., et al. (2019).
488   Different patterns of cortical maturation before and after 38 weeks gestational age demonstrated by
489   diffusion MRI in vivo. *NeuroImage* 185, 764–775. doi:10.1016/j.neuroimage.2018.05.046
490 Bozek, J., Makropoulos, A., Schuh, A., Fitzgibbon, S., Wright, R., Glasser, M. F., et al. (2018).
491   Construction of a neonatal cortical surface atlas using Multimodal Surface Matching in the Developing
492   Human Connectome Project. *NeuroImage* 179, 11–29. doi:10.1016/j.neuroimage.2018.06.018
493 Christiaens, D., Cordero-Grande, L., Pietsch, M., Hutter, J., Price, A. N., Hughes, E. J., et al. (2021).
494   Scattered slice SHARD reconstruction for motion correction in multi-shell diffusion MRI. *NeuroImage*
495   225, 117437. doi:10.1016/j.neuroimage.2020.117437
496 Claessens, N. H., Breur, J. M., Groenendaal, F., Wösten-van Asperen, R. M., Stegeman, R., Haas, F.,
497   et al. (2019). Brain microstructural development in neonates with critical congenital heart disease: An
498   atlas-based diffusion tensor imaging study. *NeuroImage: Clinical* 21, 101672. doi:10.1016/j.nicl.2019.
499   101672

500 Cordero-Grande, L., Hughes, E. J., Hutter, J., Price, A. N., and Hajnal, J. V. (2018). Three-dimensional
501 motion corrected sensitivity encoding reconstruction for multi-shot multi-slice MRI: Application to
502 neonatal brain imaging. *Magnetic resonance in medicine* 79, 1365–1376. doi:10.1002/mrm.26796

503 Counsell, S. J., Maalouf, E. F., Fletcher, A. M., Duggan, P., Battin, M., Lewis, H. J., et al. (2002). MR
504 imaging assessment of myelination in the very preterm brain. *American Journal of Neuroradiology* 23,
505 872–881

506 Dimitrova, R., Pietsch, M., Christiaens, D., Ciarrusta, J., Wolfers, T., Batalle, D., et al. (2020).
507 Heterogeneity in brain microstructural development following preterm birth. *Cerebral Cortex* 30,
508 4800–4810. doi:10.1093/cercor/bhaa069

509 Dubner, S. E., Rose, J., Bruckert, L., Feldman, H. M., and Travis, K. E. (2020). Neonatal white matter tract
510 microstructure and 2-year language outcomes after preterm birth. *NeuroImage: Clinical* 28, 102446.
511 doi:10.1016/j.nicl.2020.102446

512 Fedorov, A., Beichel, R., Kalpathy-Cramer, J., Finet, J., Fillion-Robin, J.-C., Pujol, S., et al. (2012). eng3D
513 Slicer as an image computing platform for the Quantitative Imaging Network. *Magnetic resonance
514 imaging* 30, 1323–1341. doi:10.1016/j.mri.2012.05.001

515 Fenchel, D., Dimitrova, R., Seidlitz, J., Robinson, E. C., Batalle, D., Hutter, J., et al. (2020). Development
516 of Microstructural and Morphological Cortical Profiles in the Neonatal Brain. *Cerebral Cortex* 30,
517 5767–5779. doi:10.1093/cercor/bhaa150

518 Feng, L., Li, H., Oishi, K., Mishra, V., Song, L., Peng, Q., et al. (2019). Age-specific gray and white
519 matter DTI atlas for human brain at 33, 36 and 39 postmenstrual weeks. *NeuroImage* 185, 685–698.
520 doi:10.1016/j.neuroimage.2018.06.069

521 Forsberg, D., Rathi, Y., Bouix, S., Wassermann, D., Knutsson, H., and Westin, C. F. (2011). Improving
522 registration using multi-channel diffeomorphic demons combined with certainty maps. In *MBIA*. vol.
523 7012 LNCS, 19–26

524 Girard, N., Dory-Lautrec, P., Koob, M., and Dediu, A. (2012). MRI assessment of neonatal brain maturation.
525 *Imaging in Medicine* 4, 613–632

526 Glasser, M. F. and Van Essen, D. C. (2011). engMapping human cortical areas in vivo based on myelin
527 content as revealed by T1- and T2-weighted MRI. *The Journal of neuroscience : the official journal of
528 the Society for Neuroscience* 31, 11597–11616. doi:10.1523/JNEUROSCI.2180-11.2011

529 Hermoye, L., Saint-Martin, C., Cosnard, G., Lee, S.-K., Kim, J., Nassogne, M.-C., et al. (2006). Pediatric
530 diffusion tensor imaging: normal database and observation of the white matter maturation in early
531 childhood. *NeuroImage* 29, 493–504. doi:10.1016/j.neuroimage.2005.08.017

532 Hughes, E. J., Winchman, T., Padormo, F., Teixeira, R., Wurie, J., Sharma, M., et al. (2017). A dedicated
533 neonatal brain imaging system. *Magnetic resonance in medicine* 78, 794–804. doi:10.1002/mrm.26462

534 Hutter, J., Tournier, J. D., Price, A. N., Cordero-Grande, L., Hughes, E. J., Malik, S., et al. (2018).
535 Time-efficient and flexible design of optimized multishell HARDI diffusion. *Magnetic Resonance in
536 Medicine* 79, 1276–1292

537 Iida, K., Takashima, S., and Ueda, K. (1995). Immunohistochemical study of myelination and
538 oligodendrocyte in infants with periventricular leukomalacia. *Pediatric neurology* 13, 296–304

539 Jeurissen, B., Leemans, A., Tournier, J. D., Jones, D. K., and Sijbers, J. (2013). Investigating the prevalence
540 of complex fiber configurations in white matter tissue with diffusion magnetic resonance imaging.
541 *Human Brain Mapping* 34, 2747–2766. doi:10.1002/hbm.22099

542 Jeurissen, B., Tournier, J. D., Dhollander, T., Connelly, A., and Sijbers, J. (2014). Multi-tissue constrained
543 spherical deconvolution for improved analysis of multi-shell diffusion MRI data. *NeuroImage* 103,
544 411–426. doi:10.1016/j.neuroimage.2014.07.061

Kaden, E., Kruggel, F., and Alexander, D. C. (2016). Quantitative mapping of the per-axon diffusion coefficients in brain white matter. *Magnetic Resonance in Medicine* 75, 1752–1763. doi:10.1002/mrm. 25734

Kersbergen, K. J., Leemans, A., Groenendaal, F., van der Aa, N. E., Viergever, M. A., de Vries, L. S., et al. (2014). Microstructural brain development between 30 and 40 weeks corrected age in a longitudinal cohort of extremely preterm infants. *NeuroImage* 103, 214–224. doi:10.1016/j.neuroimage.2014.09.039

Kimpton, J. A., Batalle, D., Barnett, M. L., Hughes, E. J., Chew, A. T., Falconer, S., et al. (2020). Diffusion magnetic resonance imaging assessment of regional white matter maturation in preterm neonates. *Neuroradiology* doi:10.1007/s00234-020-02584-9

Knight, M. J., Smith-Collins, A., Newell, S., Denbow, M., and Kauppinen, R. A. (2018). Cerebral White Matter Maturation Patterns in Preterm Infants: An MRI T2 Relaxation Anisotropy and Diffusion Tensor Imaging Study. *Journal of Neuroimaging* 28, 86–94. doi:10.1111/jon.12486

Kostović, I. and Judaš, M. (2006). Prolonged coexistence of transient and permanent circuitry elements in the developing cerebral cortex of fetuses and preterm infants. *Developmental Medicine and Child Neurology* 48, 388–393. doi:10.1017/S0012162206000831

Krishnan, M. L., Wang, Z., Silver, M., Boardman, J. P., Ball, G., Counsell, S. J., et al. (2016). Possible relationship between common genetic variation and white matter development in a pilot study of preterm infants. *Brain and Behavior* 6, 1–14. doi:10.1002/brb3.434

Kuklisova-Murgasova, M., Aljabar, P., Srinivasan, L., Counsell, S. J., Doria, V., Serag, A., et al. (2011). A dynamic 4D probabilistic atlas of the developing brain. *NeuroImage* 54, 2750–2763

Kuklisova-Murgasova, M., Quaghebeur, G., Rutherford, M. A., Hajnal, J. V., and Schnabel, J. A. (2012). Reconstruction of fetal brain MRI with intensity matching and complete outlier removal. *Med Image Analysis* 16, 1550–1564

Kulikova, S., Hertz-Pannier, L., Dehaene-Lambertz, G., Buzmakov, A., Poupon, C., and Dubois, J. (2015). Multi-parametric evaluation of the white matter maturation. *Brain Structure and Function* 220, 3657–3672. doi:10.1007/s00429-014-0881-y

Kunz, N., Zhang, H., Vasung, L., O'Brien, K. R., Assaf, Y., Lazeyras, F., et al. (2014). Assessing white matter microstructure of the newborn with multi-shell diffusion MRI and biophysical compartment models. *NeuroImage* 96, 288–299. doi:10.1016/j.neuroimage.2014.03.057

Makropoulos, A., Aljabar, P., Wright, R., Hüning, B., Merchant, N., Arichi, T., et al. (2016). Regional growth and atlasing of the developing human brain. *NeuroImage* 125, 456–478. doi:10.1016/j. neuroimage.2015.10.047

Makropoulos, A., Gousias, I. S., Ledig, C., Aljabar, P., Serag, A., Hajnal, J. V., et al. (2014). engAutomatic whole brain MRI segmentation of the developing neonatal brain. *IEEE transactions on medical imaging* 33, 1818–1831. doi:10.1109/TMI.2014.2322280

Makropoulos, A., Robinson, E. C., Schuh, A., Wright, R., Fitzgibbon, S., Bozek, J., et al. (2018). The developing human connectome project: A minimal processing pipeline for neonatal cortical surface reconstruction. *NeuroImage* 173, 88–112. doi:https://doi.org/10.1016/j.neuroimage.2018.01.054

Marquand, A. F., Rezek, I., Buitelaar, J., and Beckmann, C. F. (2016). Understanding Heterogeneity in Clinical Cohorts Using Normative Models: Beyond Case-Control Studies. *Biological Psychiatry* 80, 552–561. doi:10.1016/j.biopsych.2015.12.023

Morel, B., Bertault, P., Favrais, G., Tavernier, E., Tosello, B., Bednarek, N., et al. (2020). Automated brain MRI metrics in the EPIRMEX cohort of preterm newborns: Correlation with the neurodevelopmental outcome at 2 years. *Diagnostic and Interventional Imaging* doi:10.1016/j.diii.2020.10.009

Oishi, K., Chang, L., and Huang, H. (2019). Baby brain atlases. *NeuroImage* 185, 865–880. doi:10.1016/j. neuroimage.2018.04.003

Oishi, K., Mori, S., Donohue, P. K., Ernst, T., Anderson, L., Buchthal, S., et al. (2011). Multi-Contrast Human Neonatal Brain Atlas: Application to Normal Neonate Development Analysis. *NeuroImage* 56, 8–20

O'Muircheartaigh, J., Robinson, E. C., Pietsch, M., Wolfers, T., Aljabar, P., Grande, L. C., et al. (2020). Modelling brain development to detect white matter injury in term and preterm born neonates. *Brain* 143, 467–479. doi:10.1093/brain/awz412

Pannek, K., Fripp, J., George, J. M., Fiori, S., Colditz, P. B., Boyd, R. N., et al. (2018). Fixel-based analysis reveals alterations is brain microstructure and macrostructure of preterm-born infants at term equivalent age. *NeuroImage: Clinical* 18, 51–59. doi:10.1016/j.nicl.2018.01.003

Pannek, K., Hatzigeorgiou, X., Colditz, P. B., and Rose, S. (2013). Assessment of Structural Connectivity in the Preterm Brain at Term Equivalent Age Using Diffusion MRI and T2 Relaxometry: A Network-Based Analysis. *PLoS ONE* 8. doi:10.1371/journal.pone.0068593

Pecheva, D., Tournier, J. D., Pietsch, M., Christiaens, D., Batalle, D., Alexander, D. C., et al. (2019). Fixel-based analysis of the preterm brain: Disentangling bundle-specific white matter microstructural and macrostructural changes in relation to clinical risk factors. *NeuroImage: Clinical* 23, 101820. doi:10.1016/j.nicl.2019.101820

Pecheva, D., Yushkevich, P., Batalle, D., Hughes, E., Aljabar, P., Wurie, J., et al. (2017). A tract-specific approach to assessing white matter in preterm infants. *NeuroImage* 157, 675–694. doi:10.1016/j. neuroimage.2017.04.057

Pietsch, M., Raffelt, D., Dhollander, T., and Tournier, J.-D. (2017). Multi-contrast diffeomorphic non-linear registration of orientation density functions. In *ISMRM*

Pietsch, M. et al. (2019). A framework for multi-component analysis of diffusion MRI data over the neonatal period. *NeuroImage* 186, 321–337

Pittet, M. P., Vasung, L., Huppi, P. S., and Merlini, L. (2019). Newborns and preterm infants at term equivalent age: A semi-quantitative assessment of cerebral maturity. *NeuroImage: Clinical* 24, 102014. doi:10.1016/j.nicl.2019.102014

Raffelt, D., Tournier, J. D., Crozier, S., Connelly, A., and Salvado, O. (2012). Reorientation of fiber orientation distributions using apodized point spread functions. *MR in Medicine* 67, 844–855

Raffelt, D., Tournier, J.-D., Fripp, J., Crozier, S., Connelly, A., and Salvado, O. (2011). Symmetric diffeomorphic registration of fibre orientation distributions. *NeuroImage* 56, 1171–80

Raffelt, D. A., Tournier, J. D., Smith, R. E., Vaughan, D. N., Jackson, G., Ridgway, G. R., et al. (2017). Investigating white matter fibre density and morphology using fixel-based analysis. *NeuroImage* 144, 58–73. doi:10.1016/j.neuroimage.2016.09.029

Rose, J., Vassar, R., Cahill-Rowley, K., Stecher Guzman, X., Hintz, S. R., Stevenson, D. K., et al. (2014). Neonatal physiological correlates of near-term brain development on MRI and DTI in very-low-birth-weight preterm infants. *NeuroImage: Clinical* 5, 169–177. doi:10.1016/j.nicl.2014.05.013

RStudio Team (2020). *RStudio: Integrated Development Environment for R*. RStudio, PBC., Boston, MA

Rutherford, M., Biarge, M. M., Allsop, J., Counsell, S., and Cowan, F. (2010). MRI of perinatal brain injury. *Pediatric Radiology* 40, 819–833. doi:10.1007/s00247-010-1620-z

Schuh, A., Deprez, M., Makropoulos, A., Ledig, C., Counsell, S., V Hajnal, J., et al. (2014). Construction of a 4D Brain Atlas and Growth Model Using Diffeomorphic Registration. In *STIA*. vol. LNCS 8682

633 Schuh, A., Makropoulos, A., Robinson, E. C., Cordero-Grande, L., Hughes, E., Hutter, J., et al. (2018).
634 Unbiased construction of a temporally consistent morphological atlas of neonatal brain development.
635 *bioRxiv* doi:10.1101/251512

636 Schwartz, E., Kasprian, G., Jakab, A., Prayer, D., Schöpf, V., and Langs, G. (2016). Modeling fetal cortical
637 expansion using graph-regularized Gompertz models. *Lecture Notes in Computer Science (including*
638 *subseries Lecture Notes in Artificial Intelligence and Lecture Notes in Bioinformatics)* 9900 LNCS,
639 247–254. doi:10.1007/978-3-319-46720-7_29

640 Serag, A., Aljabar, P., Ball, G., Counsell, S. J., Boardman, J. P., Rutherford, M. A., et al. (2012).
641 Construction of a consistent high-definition spatio-temporal atlas of the developing brain using adaptive
642 kernel regression. *NeuroImage* 59, 2255–2265

643 Smith, S. M., Jenkinson, M., Johansen-Berg, H., Rueckert, D., Nichols, T. E., Mackay, C. E., et al.
644 (2006). Tract-based spatial statistics: Voxelwise analysis of multi-subject diffusion data. *NeuroImage* 31,
645 1487–1505. doi:https://doi.org/10.1016/j.neuroimage.2006.02.024

646 Thompson, D. K., Kelly, C. E., Chen, J., Beare, R., Alexander, B., Seal, M. L., et al. (2019).
647 Characterisation of brain volume and microstructure at term-equivalent age in infants born across
648 the gestational age spectrum. *NeuroImage: Clinical* 21, 101630. doi:10.1016/j.nicl.2018.101630

649 Tournier, J. D., Calamante, F., and Connelly, A. (2007). Robust determination of the fibre orientation
650 distribution in diffusion MRI: Non-negativity constrained super-resolved spherical deconvolution.
651 *NeuroImage* 35, 1459–1472. doi:10.1016/j.neuroimage.2007.02.016

652 Tournier, J.-D., Calamante, F., and Connelly, A. (2010). Improved probabilistic streamlines tractography
653 by 2nd order integration over fibre orientation distributions. In *ISMRM 2010*. 1670

654 Tournier, J.-D., Christiaens, D., Hutter, J., Price, A. N., Cordero-Grande, L., Hughes, E., et al. (2020).
655 A data-driven approach to optimising the encoding for multi-shell diffusion MRI with application to
656 neonatal imaging. *NMR in Biomedicine* 33, e4348. doi:https://doi.org/10.1002/nbm.4348

657 Tournier, J.-D., Smith, R. E., Raffelt, D., Tabbara, R., Dhollander, T., Pietsch, M., et al. (2019). MRtrix3: A
658 fast, flexible and open software framework for medical image processing and visualisation. *Neuroimage*
659 202, 116–137. doi:10.1101/551739

660 Uus, A., Pietsch, M., Grigorescu, I., Christiaens, D., Tournier, J.-D., Grande, L. C., et al. (2020). Multi-
661 channel Registration for Diffusion MRI: Longitudinal Analysis for the Neonatal Brain. In *Biomedical*
662 *Image Registration*, eds. Ž. Špiclin, J. McClelland, J. Kybic, and O. Goksel (Cham: Springer International
663 Publishing), 111–121

664 Wang, S., Ledig, C., Hajnal, J. V., Counsell, S. J., Schnabel, J. A., and Deprez, M. (2019). Quantitative
665 assessment of myelination patterns in preterm neonates using T2-weighted MRI. *Scientific Reports* 9,
666 1–12. doi:10.1038/s41598-019-49350-3

667 Wright, R., Kyriakopoulou, V., Ledig, C., Rutherford, M. A., Hajnal, J. V., Rueckert, D., et al. (2014).
668 Automatic quantification of normal cortical folding patterns from fetal brain MRI. *NeuroImage* 91,
669 21–32. doi:10.1016/j.neuroimage.2014.01.034

670 Wu, D., Chang, L., Akazawa, K., Oishi, K., Skranes, J., Ernst, T., et al. (2017). Mapping the Critical
671 Gestational Age at Birth that Alters Brain Development in Preterm-born Infants using Multi-Modal MRI.
672 *NeuroImage* 149, 33–43

673 Young, J. M., Vandewouw, M. M., Morgan, B. R., Smith, M. L., Sled, J. G., and Taylor, M. J. (2018).
674 Altered white matter development in children born very preterm. *Brain Structure and Function* 223,
675 2129–2141. doi:10.1007/s00429-018-1614-4

676 Zhang, H., Schneider, T., Wheeler-Kingshott, C. A., and Alexander, D. C. (2012). NODDI: Practical in
677 vivo neurite orientation dispersion and density imaging of the human brain. *NeuroImage* 61, 1000–1016.

678 doi:10.1016/j.neuroimage.2012.03.072

679 Zhang, Y., Shi, F., Yap, P. T., and Shen, D. (2016). Detail-preserving construction of neonatal brain atlases
680 in space-frequency domain. *Human Brain Mapping* 37, 2133–2150. doi:10.1002/hbm.23160

681 Zollei, L., Jaimes, C., Saliba, E., Grant, P. E., and Yendiki, A. (2019). TRActs Constrained by UnderLying
682 INfant Anatomy(TRACULInA): An Automated Probabilistic Tractography Tool with Anatomical Priors
683 for Use in the Newborn Brain. *Neuroimage* October 01, 1–17. doi:10.1016/j.neuroimage.2019.05.051.
684 TRActs